AD-A136 396 PHENOMENOLOGY OF STRUCTURED PLASMA IN THE IONOSPHERE 1/2
(U) SRI INTERNATIONAL MENLO PARK CA J F VICKREY ET AL.
01 MAR 83 DNA-TR-82-104 DNA001-82-C-0021

UNCLASSIFIED F/G 4/1 NL

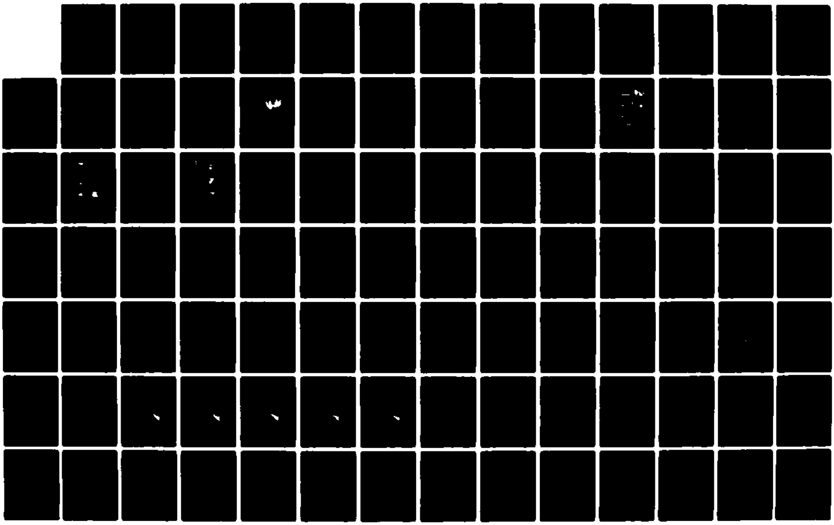

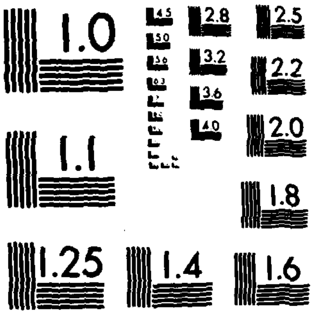

MICROCOPY RESOLUTION TEST CHART
NATIONAL BUREAU OF STANDARDS-1963-A

ADE 301266

12

DNA-TR-82-104

PHENOMENOLOGY OF STRUCTURED PLASMA IN THE IONOSPHERE

James F. Vickrey
Roland T. Tsunoda
Robert C. Livingston
Robert M. Robinson
Michael D. Cousins
Nancy B. Walker
Charles L. Rino
SRI International
333 Ravenswood Avenue
Menlo Park, California 94025

1 March 1983

Technical Report

CONTRACT No. DNA 001-82-C-0021

APPROVED FOR PUBLIC RELEASE;
DISTRIBUTION UNLIMITED.

THIS WORK WAS SPONSORED BY THE DEFENSE NUCLEAR AGENCY
UNDER RDT&E RMSS CODE B322082466 I25AAXYX00015 H2590D.

Prepared for
Director
DEFENSE NUCLEAR AGENCY
Washington, DC 20305

UNCLASSIFIED

SECURITY CLASSIFICATION OF THIS PAGE (When Data Entered)

REPORT DOCUMENTATION PAGE		READ INSTRUCTIONS BEFORE COMPLETING FORM
1. REPORT NUMBER DNA-TR-82-104	2. GOVT ACCESSION NO. AD-A136 396	3. RECIPIENT'S CATALOG NUMBER
4. TITLE (and Subtitle) PHENOMENOLOGY OF STRUCTURED PLASMA IN THE IONOSPHERE		5. TYPE OF REPORT & PERIOD COVERED Technical Report 6. PERFORMING ORG. REPORT NUMBER SRI Project 3984
7. AUTHOR(s) James F. Vickrey Roland T. Tsunoda Robert C. Livingston Robert M. Robinson	Michael D. Cousins Nancy B. Walker Charles L. Rino	8. CONTRACT OR GRANT NUMBER(s) DNA 001-82-C-0021
9. PERFORMING ORGANIZATION NAME AND ADDRESS SRI International 333 Ravenswood Avenue Menlo Park, California 94025		10. PROGRAM ELEMENT, PROJECT, TASK AREA & WORK UNIT NUMBERS Task I25AAXYX-00015
11. CONTROLLING OFFICE NAME AND ADDRESS Director Defense Nuclear Agency Washington, D.C. 20305		12. REPORT DATE 1 March 1983 13. NUMBER OF PAGES 100
14. MONITORING AGENCY NAME & ADDRESS(if different from Controlling Office)		15. SECURITY CLASS (of this report) UNCLASSIFIED 15a. DECLASSIFICATION/DOWNGRADING SCHEDULE N/A since UNCLASSIFIED

16. DISTRIBUTION STATEMENT (of this Report)

Approved for public release; distribution unlimited.

17. DISTRIBUTION STATEMENT (of the abstract entered in Block 20, if different from Report)

18. SUPPLEMENTARY NOTES

This work was sponsored by the Defense Nuclear Agency under RDT&E RMSS Code B322082466 I25AAXYX00015 H2590D.

19. KEY WORDS (Continue on reverse side if necessary and identify by block number)

Structured Plasma
Scintillation
Image Striations
Irregularity Anisotropy
Plasma Convection

20. ABSTRACT (Continue on reverse side if necessary and identify by block number)

This report summarizes the results of the past year's efforts at SRI International to investigate experimentally and theoretically the processes that control the evolution of plasma structure in the natural and the nuclear environments. Important new results include a description of the anisotropy of large-scale and scintillation-producing plasma density irregularities at high latitudes and its convection domination, the refinement of a method to

(continued)

DD FORM 1 JAN 73 1473 EDITION OF 1 NOV 65 IS OBSOLETE

UNCLASSIFIED

SECURITY CLASSIFICATION OF THIS PAGE (When Data Entered)

20. ABSTRACT (Continued)

extract true irregularity drifts from spaced-receiver measurements, the first experimental observations of the formation of image striations, a model of image formation that shows the process (in agreement with observations) to be highly scale-size selective, and evidence that the previously puzzling seasonal patterns of equatorial spread-F occurrence are a result of the seasonal changes in the time of sunset in the conjugate E layers.

EXECUTIVE SUMMARY

This report summarizes the results of an ongoing SRI International research program directed toward understanding the processes that control the evolution of plasma structure in both the natural and the nuclear environments. The major emphasis during the past year has been on high-latitude processes, because the high-latitude region is poorly understood compared with the equatorial ionosphere where the conditions and occurrance of structure development are now well established. Nevertheless, some of the theoretical developments regarding E- and F-region coupling, which were initiated because of the importance of the auroral E region, have been found to have applications to equatorial as well as barium cloud phenomena. In particular, we have shown theoretically that the formation of low-altitude image striations is highly scale-size selective. When the image formation process is driven by equatorial spread-F, the image growth rate peaks at approximately 1 km. We have shown that this is in good agreement with rocket observations of image striations at the equator. Further, these results support the speculation based on NRL simulations that E-region image striations play a role in the "freezing" of barium clouds. Such phenomena are important for determining striation lifetime and size distribution.

Another important E- to F-region coupling effect at the equator is E-region control of the occurrence of equatorial spread F. Following a suggestion of Major Leon Wittwer and Dr. Sidney Ossakow, we have shown that the seasonal peaks in equatorial spread-F activity occur during months when sunset is nearly simultaneous at the conjugate E layers. During these periods conductivity gradients are changing most rapidly.

Because nonlinear plasma phenomena couple structure at different scale sizes, the entire spectrum of plasma structure, ranging from tens of kilometers to centimeters, must be studied as a whole. This complicates the experimental picture because one must combine observations from separate experimental techniques, each of which can survey only a limited range of scale sizes. Thus, at large scales (wavelengths ⩾ 10 km), we have shown that the majority of F-layer electron density enhancements ("blobs") have limited both zonal and meridional extent. The structure observed in detail for one such blob was consistent with that expected from the gradient drift instability. In the intermediate-scale regime (wavelength ⩽ 1 km) we have shown that the irregularity anisotropy, both perpendicular and parallel to the magnetic field, has a strong latitude and local-time variation. The anisotropy appears to be controlled by the magnetospheric convection pattern.

An important experimental breakthrough made during the past year is a refinement of the spaced-receiver technique to determine simultaneously irregularity anisotropy and drift. This technique provides an inexpensive means of continuously monitoring plasma convection at high latitudes. Moreover, in conjunction with HILAT, it provides an ideal data base for refining our theoretical models of high-latitude irregularity morphology developed under DNA support.

TABLE OF CONTENTS

TABLE OF CONTENTS (Concluded)

LIST OF ILLUSTRATIONS

LIST OF ILLUSTRATIONS (Continued)

LIST OF ILLUSTRATIONS (Concluded)

LIST OF TABLES

I INTRODUCTION

The motivation for studying naturally occurring F-layer irregularities is two-fold. First and foremost, these irregularities are measurable and from their measurements we can extrapolate to the more severe propagation disturbances that will occur in a nuclear environment. In this regard, naturally occurring F-layer plasma density gradients behave like barium clouds, which have been traditionally used to simulate nuclear-produced plasma structure. The naturally formed plasma density gradients are produced at high latitudes by spatially and temporally structured particle precipitation that produces local plasma density enhancements or "blobs" in the F-region. At equatorial latitudes, gradients are formed on the edges of plasma depletions of "bubbles" formed through the Rayleigh-Taylor process.

In the case of the blob, or bubble, or barium cloud, the naturally occurring driver is small compared with the driver in the nuclear case. However, because of lower plasma temperatures in the naturally occurring driver, the diffusion rate is also much smaller. Therefore, the structure produced in barium clouds and blobs evolves in much the same way as the nuclear-produced structure. Thus, barium, equatorial bubbles, and high-latitude blobs are our outdoor laboratory test beds for models of nuclear plasma structure evolution.

The major differences among these models lie in the complexity of the plasma systems. The barium cloud is the simplest system to analyze. The input scale-size is known, the driving forces are easily determined, and the background ionosphere is reasonably well understood. The equatorial ionosphere represents the next stage of complexity. The system may have a wide range of scale sizes in different stages of evolution, as determined by nature. The drivers of structure in the F layer are neutral atmospheric winds, gravity waves, and the dynamo electric field. At high latitudes these driving processes are accompanied by destabilizing current systems, magnetospheric convection electric fields, and dynamic background ionospheric E and F layers. If a nuclear effects code were sufficiently robust to reproduce the structure observed in the high-latitude environment, it would lend confidence to its ability to predict accurately the structure resulting from a nuclear detonation.

In addition to code verification, the second motivation for studying naturally occurring plasma density irregularities is that they can hinder DoD communications and surveillance systems. Therefore, understanding the processes that control the evolution and ultimate morphology of naturally structured plasma can help to predict system performance and to develop interference mitigators.

This report summarizes the results of an ongoing SRI International research program aimed at understanding the processes that control the evolution of plasma structure in the natural and the nuclear environments. The program encompasses both theory and experiment at high and low latitudes. Moreover, because a vast range of scale sizes (tens of kilometers to centimeters) must be studied simultaneously to assess structure evolution adequately, a rich variety of complementary experimental techniques must be employed jointly. Here we will merely outline the salient results; the detailed experimental procedures and theory are contained in topical reports and papers to which we shall refer. Section II describes irregularities at polar latitudes, and Section III discusses equatorial phenomena. Section IV outlines planned future work.

II HIGH-LATITUDE F-REGION IRREGULARITIES

An important finding from the Wideband satellite experiment was the nighttime scintillation enhancement that occurs with high probability whenever the propagation path lies within the plane of the local L shell [Fremouw et al., 1977; Rino et al., 1978]. The phenomenon has been attributed to a geometrical enhancement from sheetlike irregularities. Evidence is accumulating, however, that a localized source region also contributes to the nighttime scintillation enhancement. Through combined incoherent-scatter and scintillation observations, the F-region source of the irregularities and the dynamics of the source region have been identified [Vickrey et al., 1980]. Enhanced scintillation appears to be associated with the horizontal plasma-density gradients ("walls") of localized plasma-density enhancement (blobs), in the auroral F layer.

The experimental and theoretical work that has led to our current understanding of this high-latitude phenomenon is reviewed in Rino and Vickrey [1982] and in a DNA La Jolla meeting report to be published. Because of the exceptionally good definition of the source region and its dynamics, we have concentrated on this particular source of high-latitude irregularities. The results are grouped into two scale size regimes according to the following criteria:

- The structure and anisotropy of intermediate-scale (~ 500 m to ~ 10 km) irregularities that are the primary contributors to the scintillation.
- The structure, morphology, and likely source mechanisms of large-scale (> 10 km) F-region density enhancements.

The physical processes that couple the large- and small-scale irregularities are discussed in detail in Kelley et al. [1982] and Vickrey and Kelley [1982a], and have been reviewed by Vickrey [1982] and Vickrey and Kelley [1982b]. These authors have presented a framework for understanding high-latitude irregularities that consists of (1) a simple source function of irregularities, (2) a model of the scale-size dependent lifetime of irregularities that depends on E-region conductivity, and (3) a model of high-latitude convection that redistributes irregularities throughout the polar regions. Although this framework is straightforward, it has led to more extensive experiments that have revealed the complexity of each element. In the following two sections, we highlight the pertinent results of some of those experiments.

A. Intermediate-Scale Auroral F-Region Irregularities

During the active measurement phase of the Wideband satellite experiment (May 1976 to August 1979), spaced-receiver measurements were made to resolve unambiguously the anisotropy and drift of the irregularities. An elaborate data analysis procedure must be used for such measurements [Rino and Livingston, 1982] but the results that are now emerging seem to justify the effort. However, before presenting some of these results, we emphasize that the correlation method is most sensitive to kilometer-scale structures. Ultimately, we would like to know the scale-size or spatial wavelength dependence of the anisotropy and drifts.

Livingston et al. [1982] have carefully measured the variation of the axial ratio and orientation angle of the diffraction pattern during a large number of satellite passes. They were able to identify systematic transitions among three generic types of irregularity structures: rods, winds, and sheets. Rods are isotropic in the plane transverse to the geomagnetic field and can be characterized by an axial ratio (aprallel to transverse dimensions) of a:1. Wings and sheets are elongated both along the geomagnetic field and in the transverse plane along the direction of the local L shell and are characterized by two axial ratio parameters as a:b:1. For sheets, a=b. Wings are intermediate-scale structures with b = a/2.

Figure 1 shows the general pattern established by Livingston et al. [1982]. The contours indicate rods, and the cross-hatched regions denote sheets or wings; the values are the extension ratio, a. The axial ratio of the rods systematically decreases toward the poleward boundary of the scintillation zone, giving way to surprisingly low (nearly isotropic) values. Sheets and wings are confined to the equatorward region of the

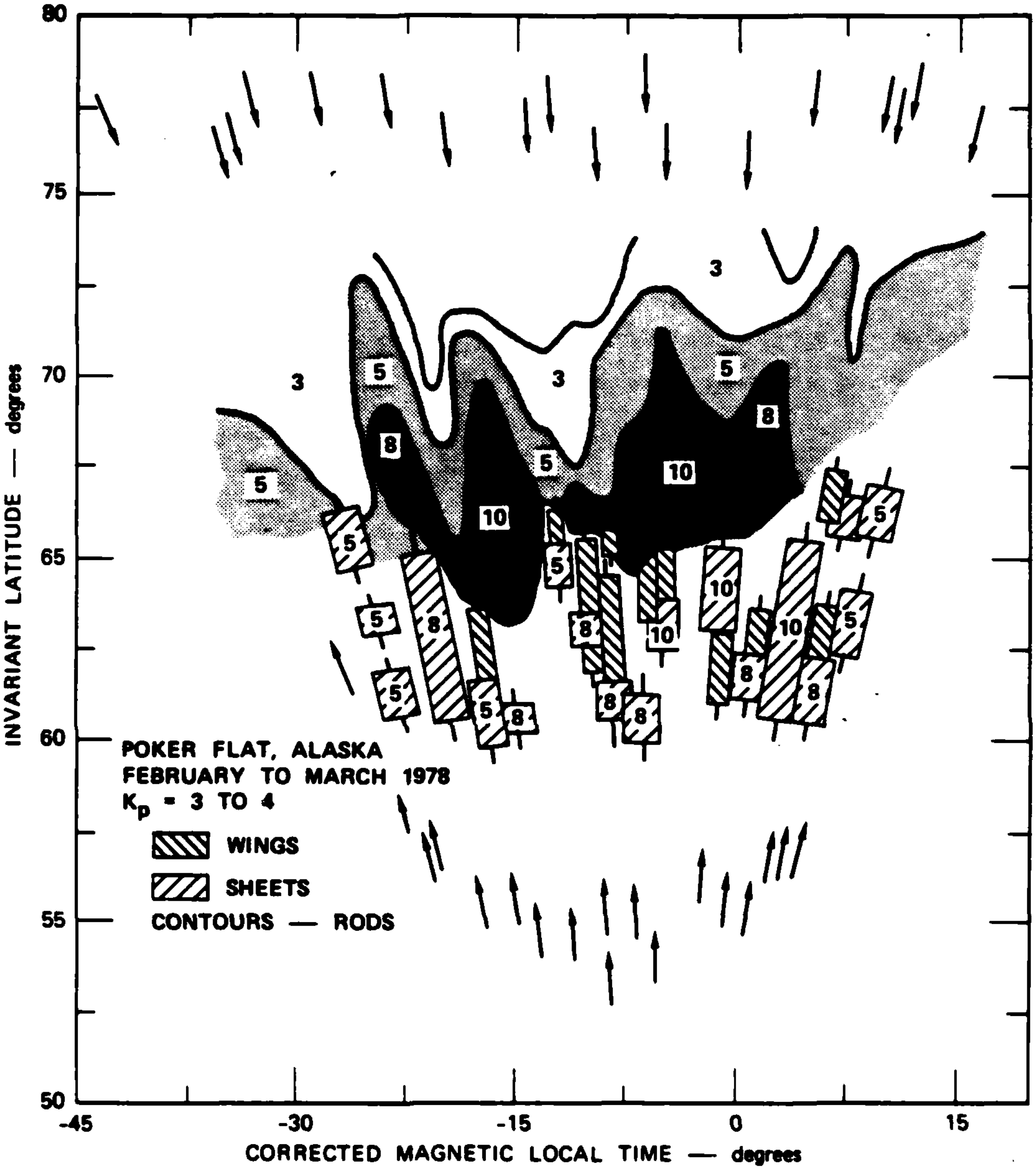

FIGURE 1 MORPHOLOGY OF IRREGULAR ANISOTROPY UNDER CONDITIONS OF MODERATE ACTIVITY. The expected large-scale convection pattern is superimposed.

scintillation zone. There is a systematic reduction in anisotropy (the rods shorten while sheets give way to wings) through magnetic midnight.

Livingston et al. [1982] showed that this pattern is closely related to the expected nighttime convection flow, as Figure 2 depicts. The general reduction in anisotropy coincides with the expected duration of the Harang discontinuity. Sheets occur only in the regions of strong electrojet flows, which suggests that convection and velocity shear are important factors in controlling the irregularity anisotropy [Vickrey and Kelley, 1982].

More recent measurements using polar beacon satellites in highly eccentric orbits provide additional evidence for the relation between convection and irregularity anisotropy (see Section III). For these satellites, the orbital velocity component is primarily along the propagation line of sight and, as such, does not strongly affect the correlation measurements.

It is therefore possible to establish irregularity drift, as well as anisotropy at a fixed penetration point. An example of anisotropy variation for a few hours of observation is shown in Figure 3 in the same format as Figure 1. These data correspond to the same magnetic conditions as Figure 1, and the local time variation is similar to that in the long-term morphological pattern. In this case, however, we have direct confirmation from the velocity data in Figure 4 that the anisotropy minimum near 2300 corresponds to the Harang discontinuity.

B. Large-Scale Auroral F-Region Irregularities

To complement the scintillation observations of intermediate-scale auroral structures just described, the Chatanika incoherent-scatter radar has been used to investigate the nature of the large-scale electron density structure found in the auroral F layer. The radar beam was scanned in elevation, usually in the magnetic meridian, to map out the spatial characteristics of this structure. The structure has been found to take the form of plasma-density enhancements, called F-region blobs. We have found that blobs are produced by two possible sources of soft-particle precipitation, and that they have longitudinal as well as latitudinal structure.

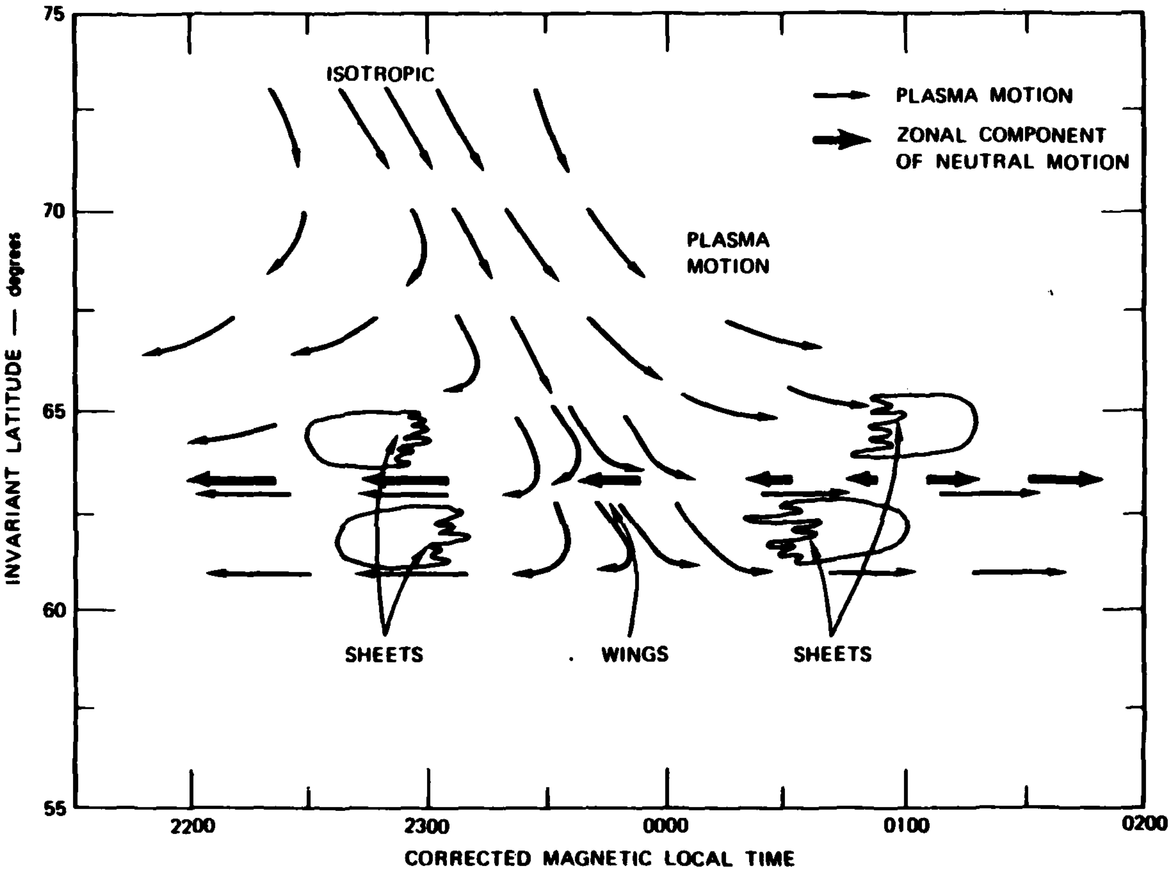

FIGURE 2 SCHEMATIC DIAGRAM OF ANISOTROPY VARIATIONS AND ITS RELATION TO AVERAGE NIGHTTIME CONVECTION PATTERN

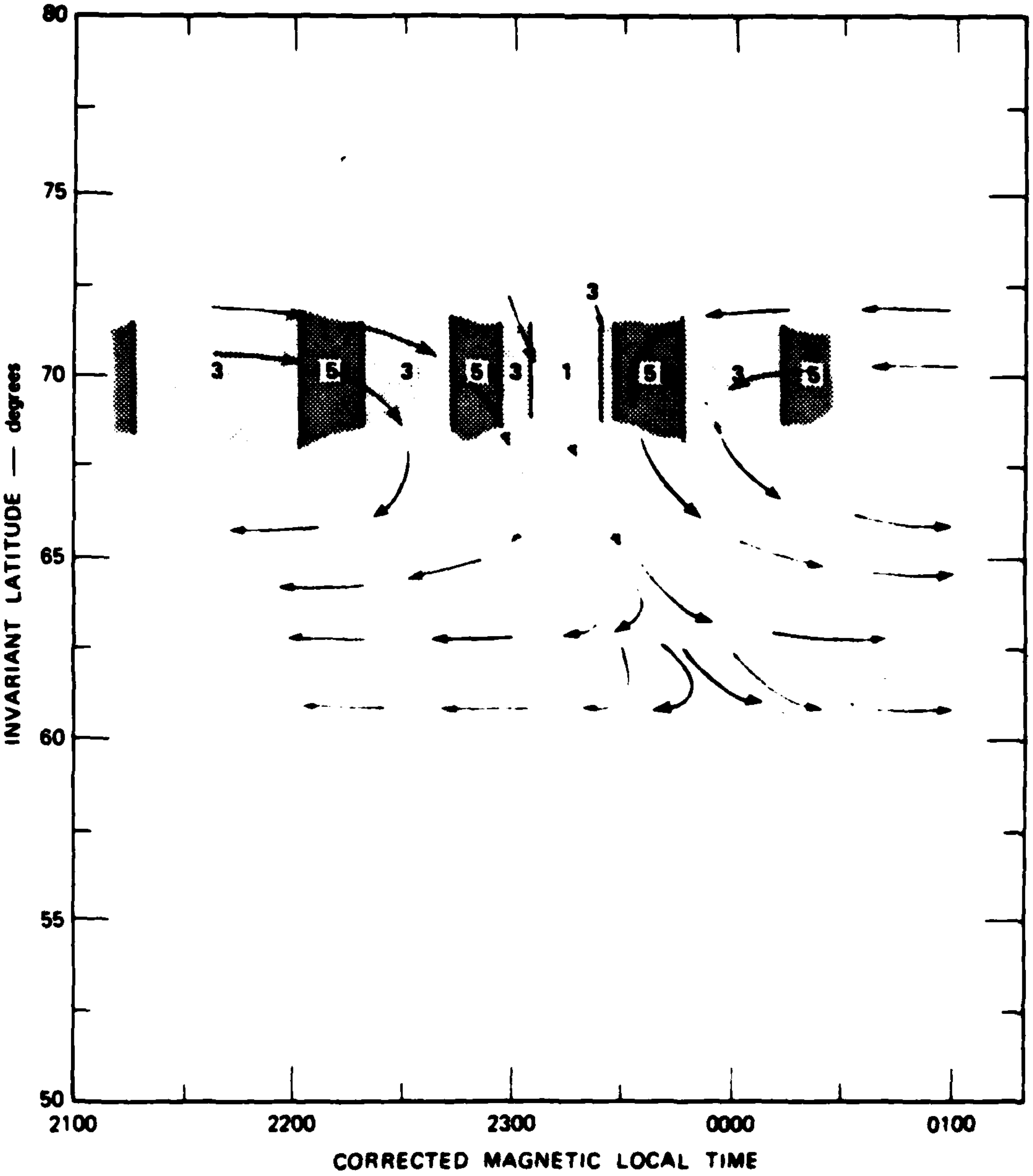

FIGURE 3 ANISOTROPY VARIATION WITH LOCAL TIME, DERIVED FROM POLAR BEACON SATELLITE DATA. The expected large-scale convection pattern is superimposed.

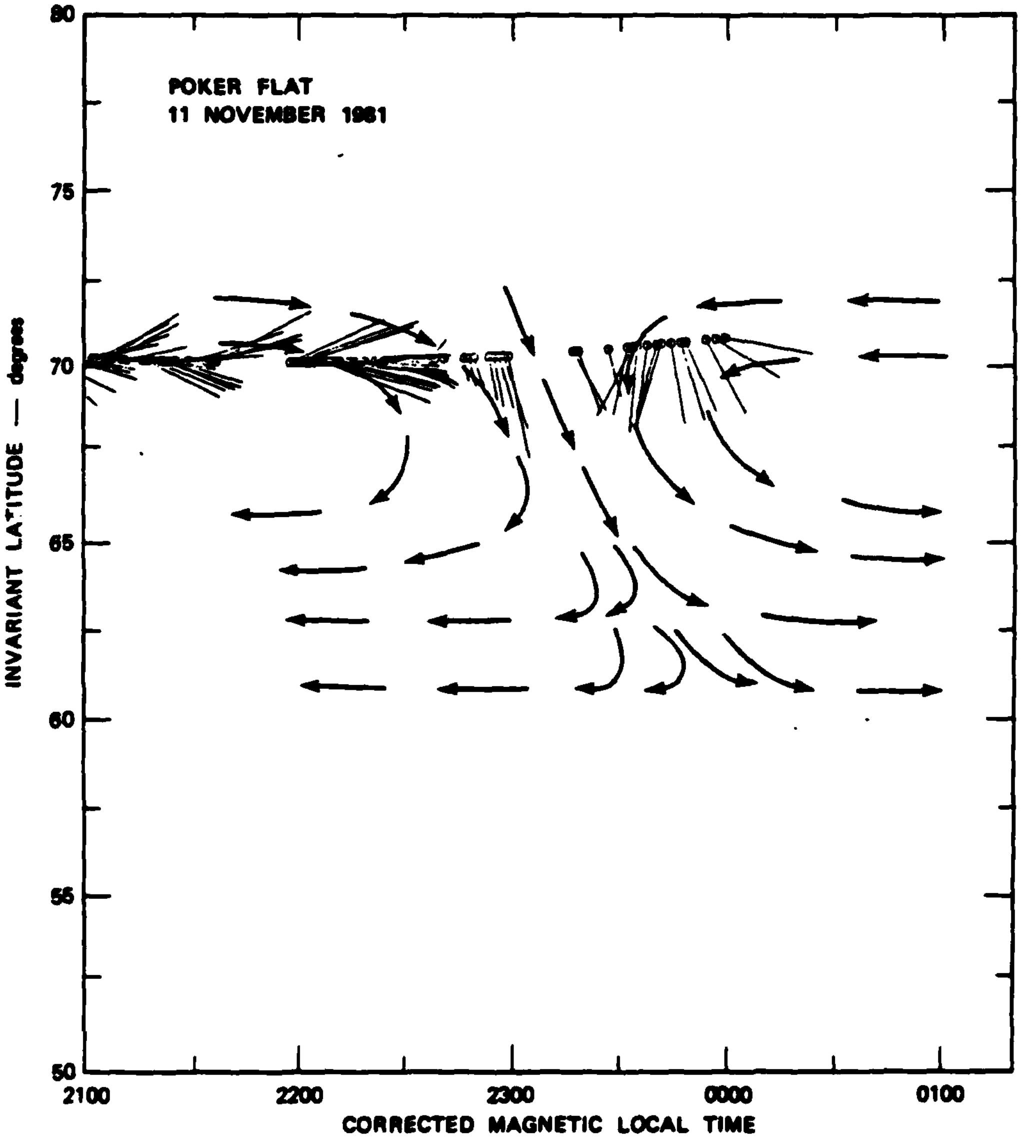

FIGURE 4 IRREGULARITY DRIFT PATTERN VARIATION WITH LOCAL TIME, DERIVED FROM POLAR BEACON SATELLITE DATA. The expected large-scale convection pattern is superimposed.

Beside specifying the polar cusp and the "soft zone" of particle precipitation [Eather, 1969] as source regions for F-region blobs [e.g., Kelley et al., 1982], we have found that at least two specific sources can be identified. We show below that the longest (in longitude) blob is located near the equatorward boundary of the auroral oval, and that the shorter blobs are located poleward of this boundary blob. Because of its characteristic location and longitudinal extent, we identify the boundary blob as a unique auroral F-region feature, distinct from the other ordinary blobs. We suggest that the source of the boundary blob is latitudinally localized precipitation of low-energy electrons from the inner edge of the central plasma sheet. We further suggest that the source of the other blobs is the inverted-V event [e.g., Frank and Ackerson, 1971].

We present in Figure 5 examples of the boundary blob in a set of four successive scans made with the Chatanika radar. The data have been plotted as isodensity contours in altitude and ground distance coordinates. The boundary blob in Figure 5 is the plasma-density (shaded) region that appears to move equatorward as a function of time. Equatorward of the boundary blob is a sunlit F layer, which is separated from the boundary blob by a narrow latitudinal region of low plasma density. Poleward of the boundary blob are the ordinary blobs. Examples of isolated blobs, like those in the third panel of Figure 5, suggest that the blobs are localized enhancements rather than depletions. The boundary blob is identified by its proximity to the equatorward boundary of the auroral oval, defined by the equatorward edge of the auroral E layer that is evident in all four of the panels in Figure 5.

The locations of the boundary blob and other blobs with peak plasma densities greater than 4×10^5 el/cm^3 have been plotted as a function of invariant latitude and magnetic local time (MLT) in Figure 6. Solid circles connected by line segments are used to show the location of the boundary blob. The longitudinal extent of the boundary blob is evident from its persistence as a function of MLT and from comparison with the sporadic appearance and disappearance of the ordinary blobs. Electric-field measurements indicate that the boundary blob is longitudinally extended and is not an isolated feature corotating with the earth. As a

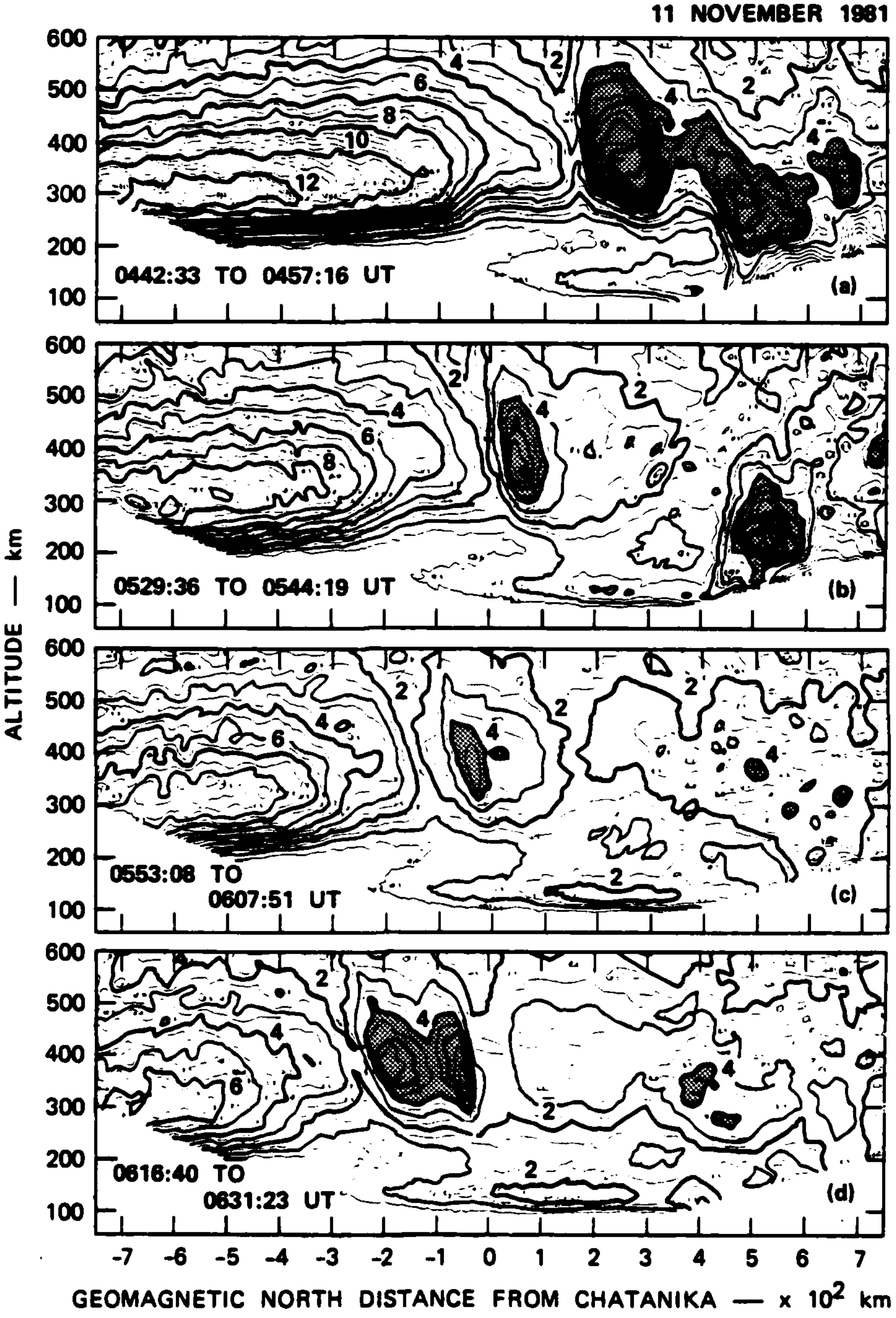

FIGURE 5 LATITUDINAL CROSS SECTIONS OF THE BOUNDARY BLOB

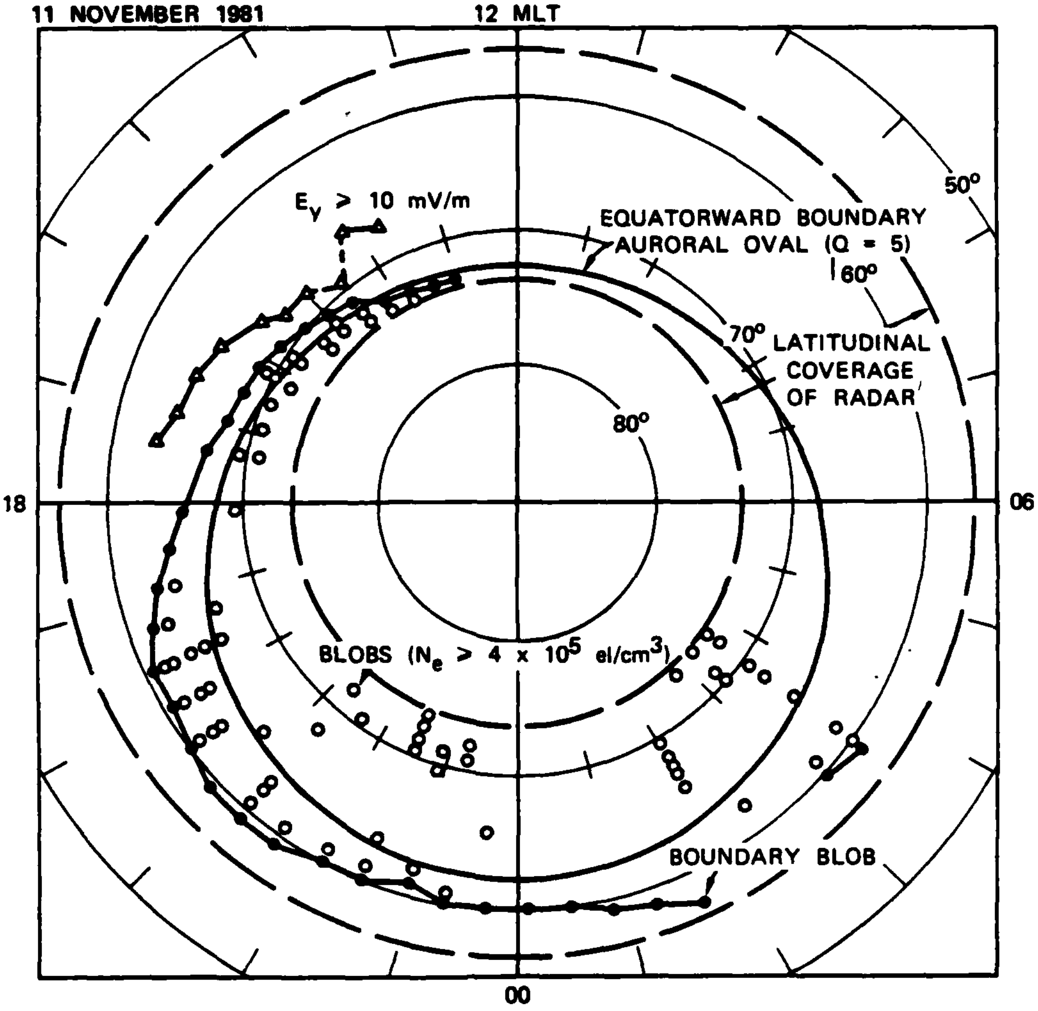

FIGURE 6 BOUNDARY BLOB LOCATION AS A FUNCTION OF INVARIANT LATITUDE AND MAGNETIC LOCAL TIME

statistical reference, we have also plotted the equatorward boundary of the auroral oval (Q = 5), as determined analytically by Starkov [1969]. We see from Figure 6 that the invariant latitude of the boundary varied as a function of MLT in a manner that more or less paralleled that of the auroral oval boundary in the afternoon and midnight sectors. The equatorward departures in the evening and postmidnight sectors appear to be associated with substorm effects.

The proposed relationship of ordinary blobs to inverted-V events appears reasonable if we consider the nature of inverted-V precipitation. Inverted-V events are characterized by an electron energy spectrum whose peak energy varies as a function of latitude from a few hundred electron volts to a few kiloelectron volts before decreasing again to a few hundred electron volts [e.g., Lin and Hoffman, 1979; Hoffman and Lin, 1980]. Their latitudinal widths vary from less than 0.5 deg to no more than 2 deg, with the most probable width occurring at the smaller values. Inverted-V events are associated with intense electron fluxes and represent the most common form of precipitation in the auroral zone. For example, Hoffman and Lin [1981] have found from Atmospheric Explorer-D satellite data that inverted-V events occurred in 94 percent of the passes analyzed, with 72 percent of those events occurring near the poleward edge of the auroral oval. The spectral characteristics of inverted-V precipitation whould produce ionospheric signatures that in altitude-latitude coordinates resemble in form an upright V. Because of more rapid loss rates at lower altitudes, the upright-V ionization form should decay into a pair of blobs. Of course, if the inverted-V event is very narrow in latitudinal width, the radar signature may be a single blob. An example of an upright-V signature is presented in Figure 7. The isodensity contours indicate the presence of an auroral arc located at an altitude of about 150 km. If the auroral arc were produced by a narrow beam of keV electrons, we would expect the plasma density to be latitudinally confined along the geomagnetic field line passing through the auroral arc, indicated by the dashed line in Figure 7. Instead, we see a plasma-density contour pattern that spreads outward latitudinally with increasing altitude, as is expected from an inverted-V event.

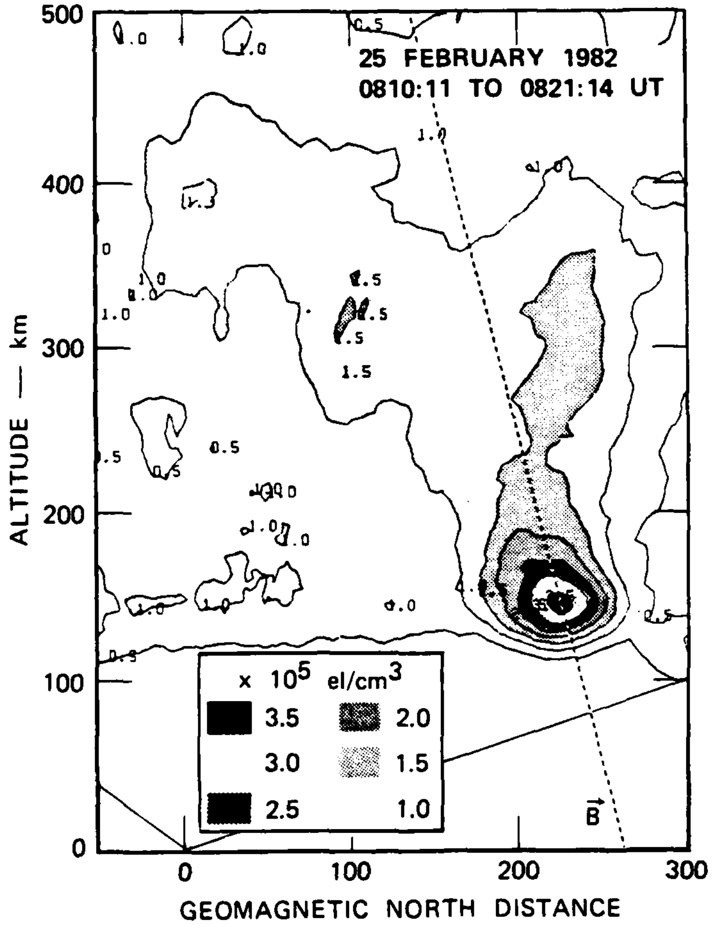

FIGURE 7 IONOSPHERIC SIGNATURE OF AN INVERTED-V EVENT

We have found that ordinary blobs can have longitudinal structure. That is, blobs are not only limited in latitudinal extent, but occasionally show variations in latitudinal cross section as a function of longitude. This longitudinal structure is consistent with plasma-density structuring by the gradient-drift instability [e.g., Linson and Workman, 1970]. However, an alternative explanation for this structure is a varying source of soft-particle precipitation. This second source, however, appears to require very large particle fluxes.

A Chatanika data set used to reveal the longitudinal structure associated with a blob is presented in Figure 8. The data set consists of six elevation scans in the magnetic meridian. The scan sector was centered on the blob and limited (compared to the full scans shown in Figure 5) so that the scans were closely spaced in time. The isodensity contour plots in Figure 8 differ from those in Figures 5 and 7 because the data were reformatted to produce a plot in which the geomagnetic field lines are vertically oriented. The vertically oriented blobs are therefore field aligned.

Evidence of longitudinal (or east-west) structure is contained in the variability of blob characteristics from map to map. From Figure 8 we see that the density structure found in successive maps does not correlate well. A blob found in one map cannot be easily identified with a blob in the next map without invoking anomalously large: production by particle precipitation, latitudinal transport by east-west electric fields, or loss rate. The most reasonable interpretation appears to be in terms of east-west structure. (Details of this data set are described in Tsunoda and Vickrey [1982].)

Interpretation of the data in Figure 8 in terms of longitudinal structure is best illustrated by plan views of the isodensity contours at selected altitudes. To make these plan views, we have taken the plasma-density variations as a function of invariant latitude, at selected altitudes (horizontal lines in the maps in Figure 8), and fitted isodensity contours to the values obtained from the six scans. The zonal displacements between scans were computed by using the measured southward electric

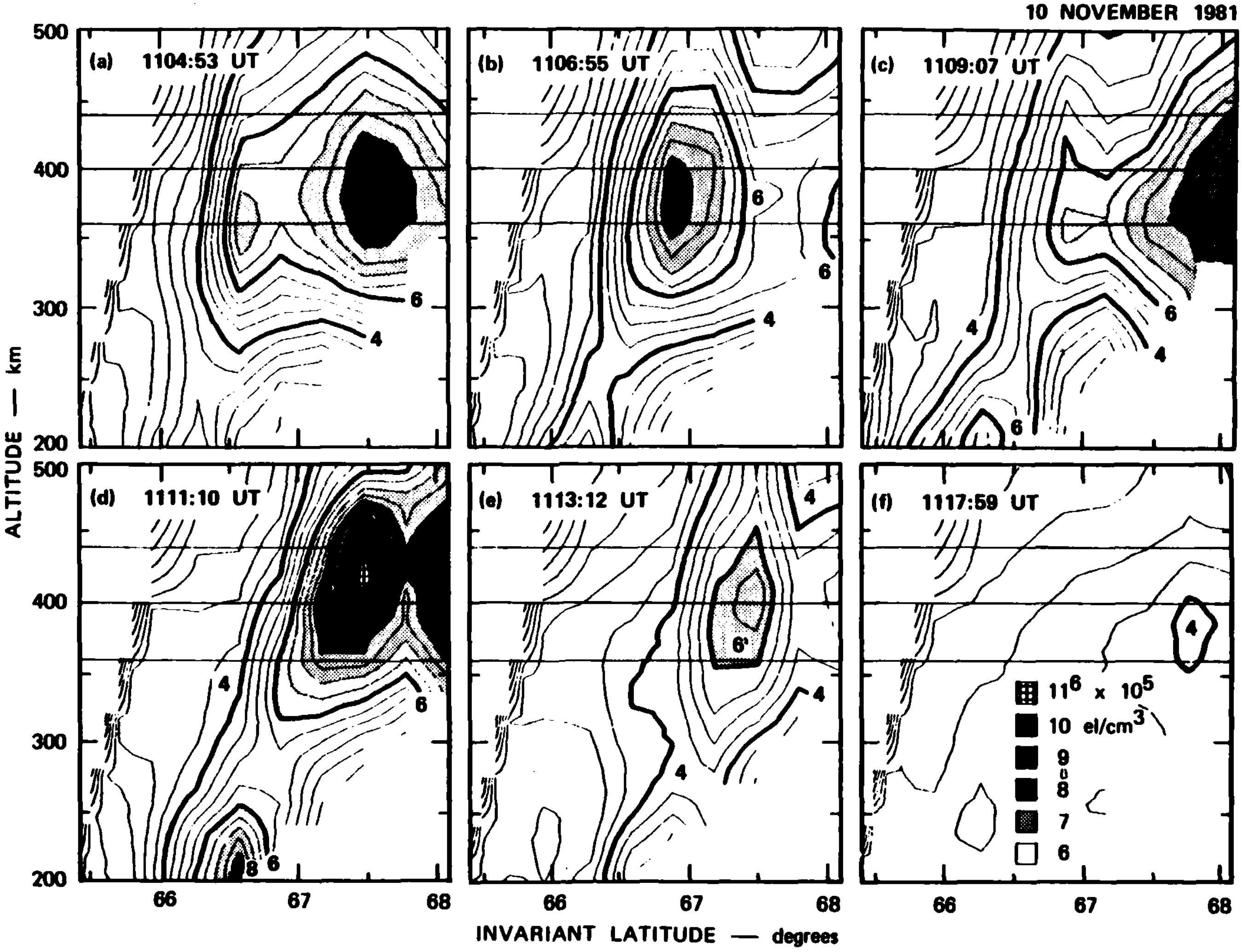

FIGURE 8 SIX MERIDIAN-SCAN MAPS OF ISODENSITY CONTOURS SHOWING THE APPARENT VARIABILITY IN BLOB PLASMA-DENSITY STRUCTURE

field of 22 mV/m. No attempt was made to compensate for any latitudinal displacement because the east-west electric field component was small. The resulting isodensity contour maps for altitudes of 360, 400, and 440 km are presented in Figure 9.

The apparently uncorrelated blob features seen in the six maps in Figure 8 are interpreted in Figure 9 as longitudinal structure associated with the equatorward wall of a large-scale blob. Two regions of enhanced plasma density have "fingers" extending southward and are separated in east-west direction by regions of depleted plasma density. Similar patterns of east-west structure are seen in the three contour maps taken at different altitudes. The east-west separation of the fingers is about 150 km. The contour maps in Figure 9 also indicate structuring of the west wall of the center finger in Figure 9. The structuring is in the form of an eastward penetration of a low plasma-density contour between two regions of higher plasma density. This structure is most evident at the 400-km altitude, although there is also some indication of the eastward penetration (of a lower valued contour) at the 360-km altitude.

The blob structure described above is consistent with that produced by the gradient-drift instability. This instability has a positive growth rate whenever the plasma drift (relative to the neutral gas) is parallel to the plasma-density gradient. In this data set, the electrodynamic conditions included a southward neutral wind of 370 m/s and a southward electric field of 22 mV/m. The neutral wind acts to structure the equatorward wall of the blob, producing the longitudinal structure just described. Similarly, the southward electric field acts to structure the west wall of the blob. Both forms of structure were observed as shown in Figure 9.

The difficulty with this interpretation is the damping effects of a conducting E layer. If the E layer connected to the blob field lines was highly conducting, the polarization electric fields that produce the structuring via flux-tube interchange would not develop. Unfortunately, the E-layer electron density was not measured in this experiment because the blob was located too far north of the radar. It is hoped that future experiments will resolve this ambiguity in interpretation.

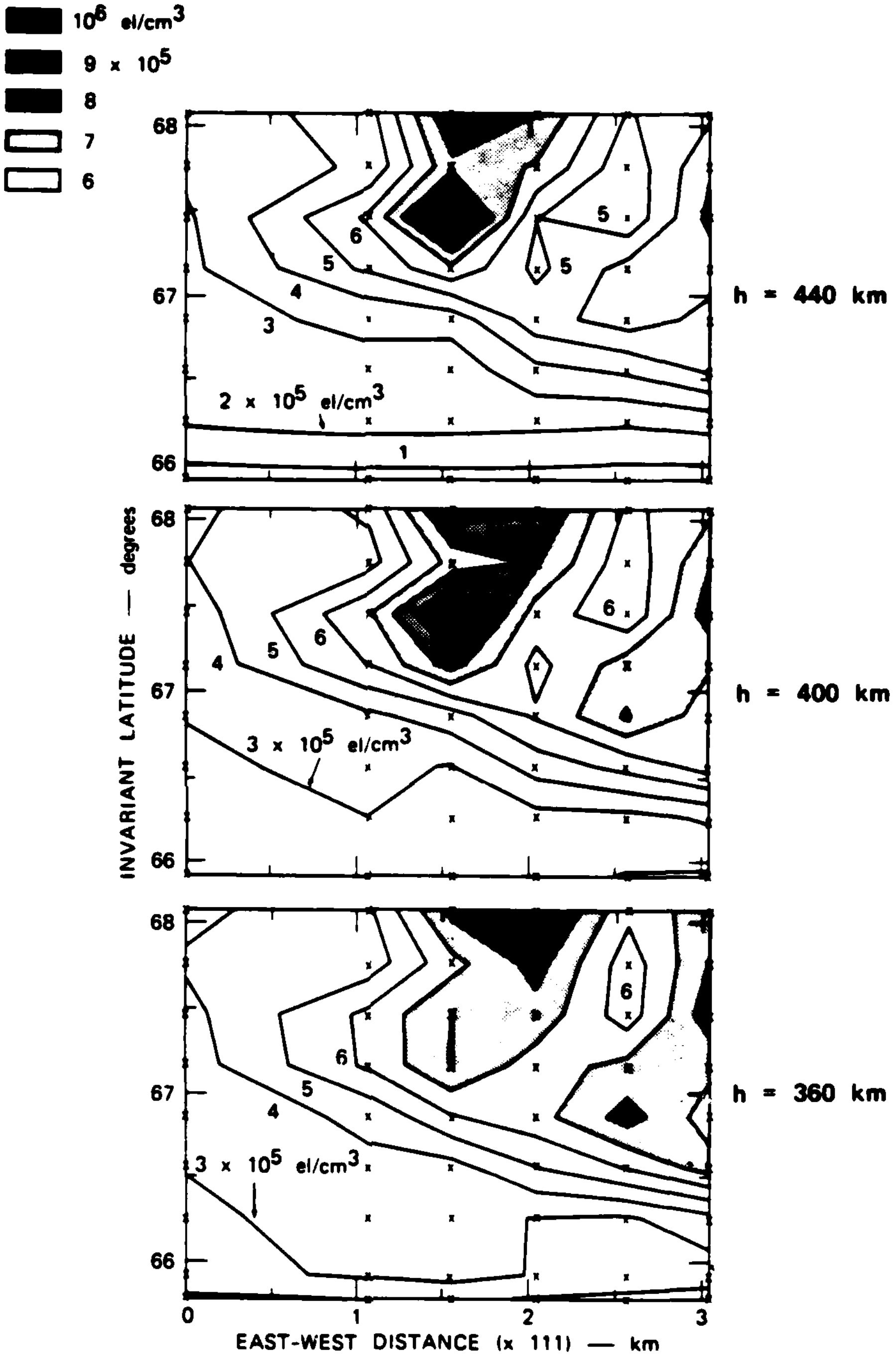

FIGURE 9 PLAN VIEWS OF BLOB EAST-WEST STRUCTURE AT THREE DIFFERENT ALTITUDES

C. Spaced-Receiver Measurements of Polar Cap Irregularity Anisotropy and Drift

The magnetic polar cap is the region of open magnetic field lines that, driven by the solar wind, extends into the tail of the magnetosphere. It is, accordingly, a region in which the structure and dynamics are closely tied to the state of the interplanetary magnetic field (IMF) and thus to the sun. This solar control is conspicuous if we consider the scintillation changes observed over the recent sunspot cycle. A measurement campaign in 1975 judged the region benign in terms of communication disruption, but in 1979 scintillation levels throughout the local winter routinely exceeded those simultaneously observed in the auroral zone [Aarons et al., 1981].

The polar cap region is interesting not only because of the severity of scintillation, but it is, very likely, a source region for the large-scale electron density structures observed in the auroral zone. Furthermore, the dynamics of the region provide a sensitive indicator of the sense and magnitude of the interplanetary magnetic field. These factors are essential to an understanding of the irregularity physics and to the eventual goal of global irregularity modeling.

Until the observations discussed here were made, there were virtually no measurements of intermediate-scale irregularity anisotropy in the polar cap. The occasional exceptions are from the early portions of Wideband satellite passes in the midnight sector and under disturbed magnetic conditions; however, the low-elevation-angle-observation geometry for these Wideband cases is far from ideal for the detailed diagnosis of irregularity shape. In contrast with this paucity of anisotropic data, there has been extensive study of plasma drift in the polar cap by both modeling and observation. Experimental concentration has been on the large-scale electric-field patterns that are mapped down from the magnetosphere. These have been implied from multiple magnetometer data [Friis-Christensen et al., 1972] or directly measured by balloon flights [Mozer and Serlin, 1969] and satellites [Heelis et al., 1982].

The polar cap plasma-flow direction is dominated by the northward (B_Z) component of the interplanetary field. Under normal conditions, B_Z is negative and small, and these characteristics cause a convection pattern in the vicinity of the magnetic pole that is two-celled, with flow from noon toward midnight and sunward return through the dawn and dusk auroral zones. Generally, the two-flow cells are asymmetric, both skewed from the noon-midnight meridian and offset from the magnetic pole. This lack of symmetry is generated by spatial or temporal changes in the eastward component of the IMF, B_Y, which controls the dawn-dusk flow component to first-order.

When B_Z turns northward, a variety of complex electric-field distributions can occur. Heppner [1972] has categorized these in terms of their dawn-dusk signatures. These range from patterns explainable by four-celled polar-cap convection to essentially random field variations throughout the entire region. Burke et al. [1979] have studied a subset of B_Z north observations and have postulated a magnetospheric mechanism for their cause.

Satellite in-situ measurements of polar-cap electric fields like those referenced above have been made using sun-synchronous dawn-dusk orbits. These measurements provide one-dimensional snapshots of the most critical features of the convection dynamics, but cannot provide simultaneous information about the field elsewhere in the polar cap. The value of the ground-based drift measurements using the polar beacons is that the drift pattern can be continuously monitored, albeit at a single point. The complementary nature of the two methods is clear and should be taken full advantage of during the HILAT program.

The data we discuss here are from an extensive spaced-receiver data set collected from Thule, Greenland. Since 1979, short spans of multiple antenna observations have been routinely made daily for several months at a time; our emphasis here is on data from several days of continuous observations made during January 1982. The diurnal drift patterns derived from these data, using signals from the UHF polar beacons, are currently being consolidated. Here we present anisotropy and drift data for one consecutive dawn, noon, and dusk sequence during which the magnetic-field conditions were nearly constant.

Dawn-sector anisotropy data for 22 January 1982 are shown in Figure 10. The lower scale on the figure is universal time; the upper scale indicates corrected MLT. Because the penetration point remains nearly constant during the observations, the two time scales are separated by a fixed amount. The invariant latitude at F-region penetration altitudes is near 85 deg, well into the central polar cap.

The ground-diffraction-pattern orientation data in the top portion of Figure 10 indicates distinctly rod-like irregularities as the cause of the scintillation. In fact, the model predictions cannot be distinguished from the measured data; those for sheet-like irregularities (not shown) differ by nearly 30 deg from the measured orientation. The irregularity extension for which two model predictions are shown is quite variable, but generally is greater than that seen in the auroral zone [Livingston et al., 1982], reaching 20:1:1 beyond 0530 UT. The corresponding dawn-sector drifts are shown in Figure 11. The drift magnitudes are high; they exceed 900 m/s slightly past 0500 UT. The magnetic north-south component systematically increases from 200 m/s to about 500 m/s southward, while the more rapidly varying east-west component averages about 400 m/s in an eastward direction. For this invariant latitude, the southeastward flow is consistent with an overall two-cell flow pattern expected for B_Z negative conditions. A comparison of Figures 10 and 11 suggests the same convective control of anisotropy observed in the auroral zone [Livingston et al., 1982]. Generally, the axial ratio follows the variations in north-south drift, minimizing when the drifts are high. The association between anisotropy and the east-west velocity component is not clear. This point will be discussed further in association with the noon- and dusk-sector data.

The local-noon-sector data correspond to nearly the same invariant latitude of 85 deg and are shown in Figures 12 and 13. The irregularities are still rod-like, but are extended over those seen in the dawn sector and exceed 50:1:1 at times. An in-situ extension of 20:1:1 is a

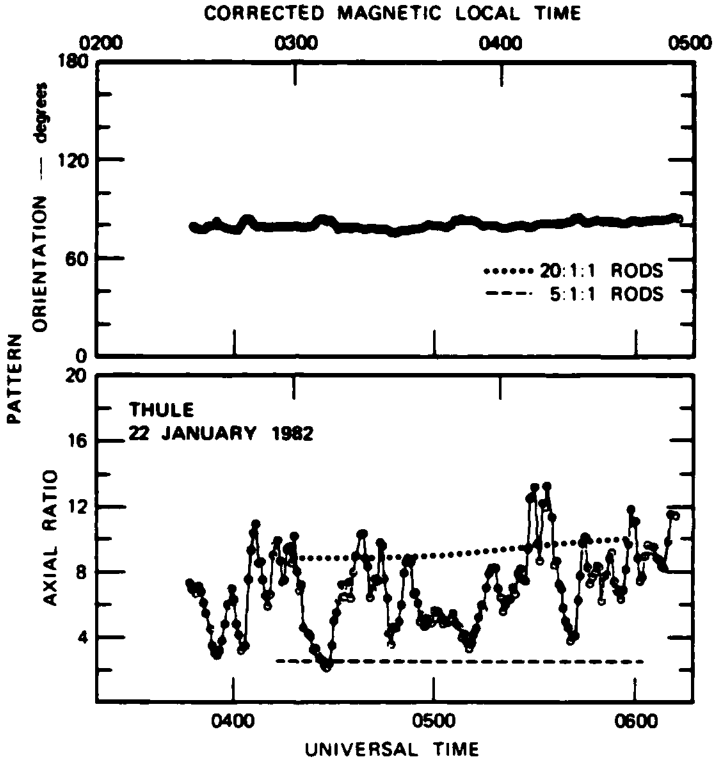

FIGURE 10 LOCAL DAWN-SECTOR ANISOTROPY DATA

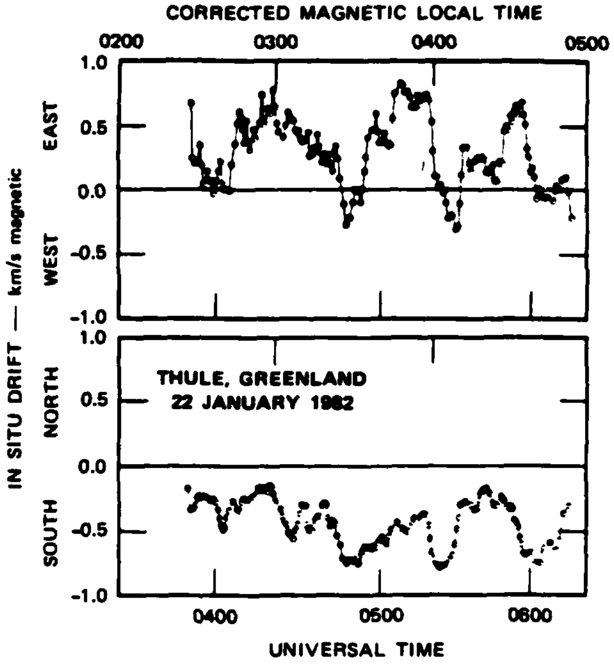

FIGURE 11 LOCAL DAWN-SECTOR DRIFTS

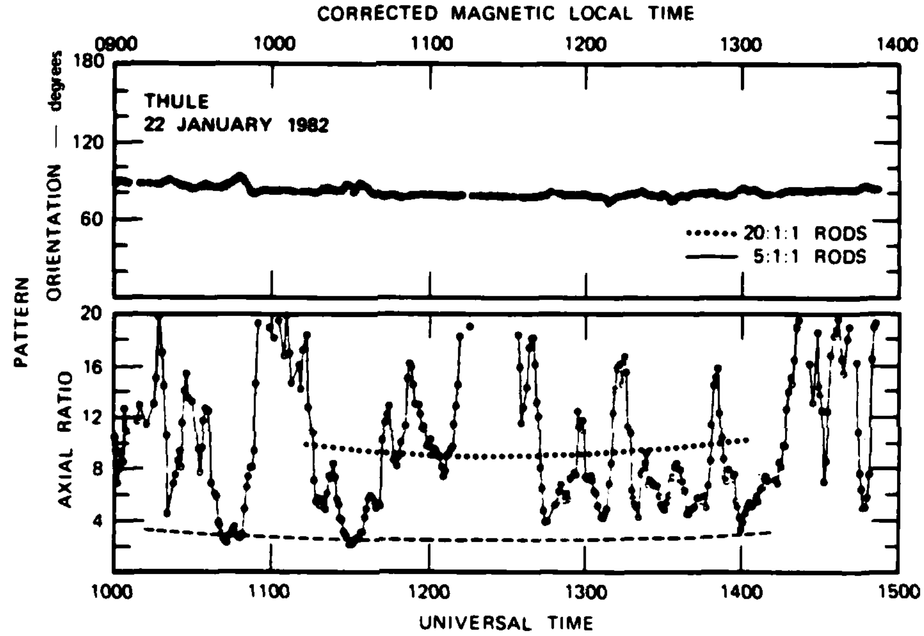

FIGURE 12 LOCAL NOON-SECTOR DATA

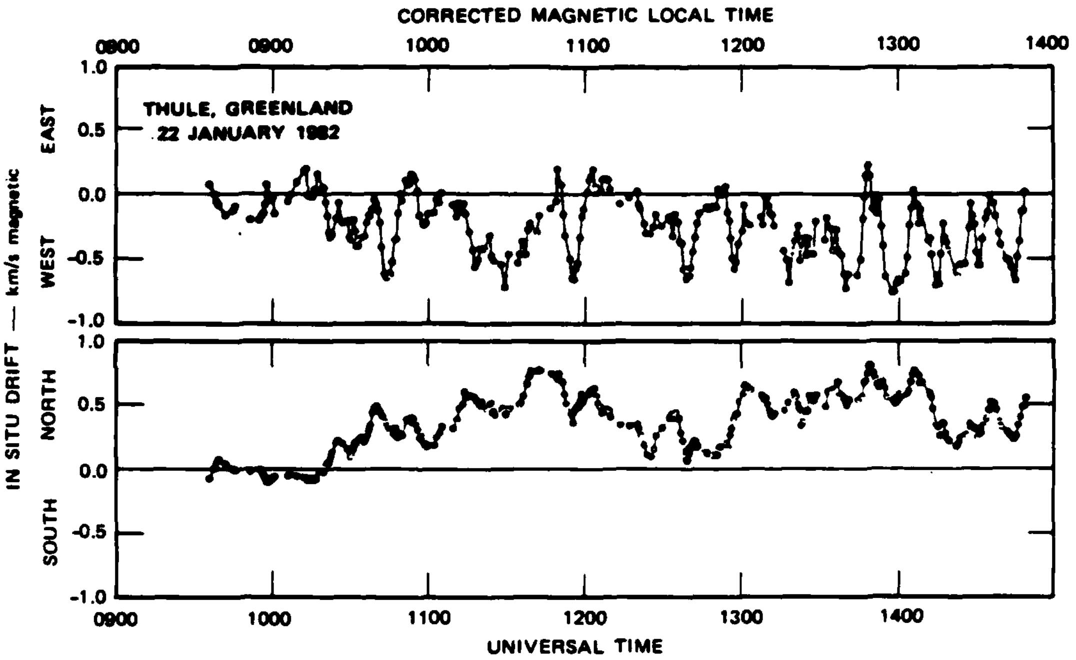

FIGURE 13 LOCAL NOON-SECTOR DATA

typical value. The axial ratio varies with a 60- to 80-min period up through 1300 UT, perhaps associated with the passage of F-region sun-aligned arcs [Weber and Buchau, 1981]. The drifts in Figure 13 are mostly antisunward, as expected in the noon sector, but also include a distinct but rapidly varying westward component. The westward component presumably arises from an asymmetry in the two-celled pattern generated by a nonzero component of B_Y. The magnitude of the drifts occasionally exceeds 800 m/s and they are therefore comparable to those observed in the dawn sector. Unlike the dawn sector, however, the variations in axial ratio are tied more closely to changes in east-west drift.

Data taken near local dusk on the same day are shown in Figures 14 and 15. The penetration latitude in this case is 86 deg, slightly northward of the other time-sector data. The irregularities are still rod-like, systematically increasing from about 20:1:1 elongation in midafternoon to about 40:1:1 by 2100 UT. This increase is associated with a general decrease in drift speed, although there is no clear association, feature-for-feature, with the northward or eastward components. The northeastward drift in this case also fits the skewed two-cell flow pattern suggested by the dawn-aand noon-sector data.

Detailed comparisons between these data and simultaneous ionosonde and optical observations are under way. Associations between particular anisotropy and drift features, and the large-scale polar-cap structures can then be established, and the process of identifying instability processes can be initiated. From these measurements alone, however, we can make some preliminary conclusions:

(1) The irregularities in the ~ 600-m spatial wavelength regime are almost exclusively rod-like and range in extension from about 5:1:1 to 50:1:1. We note that on the day following the examples shown here, deviations from the rod-like structures do occur that correspond to unusual drift flow patterns. For either irregularity type, scintillation levels for field-aligned propagation can be greatly and consistently enhanced. For the polar cap, this will be at a near-vertical geometry.

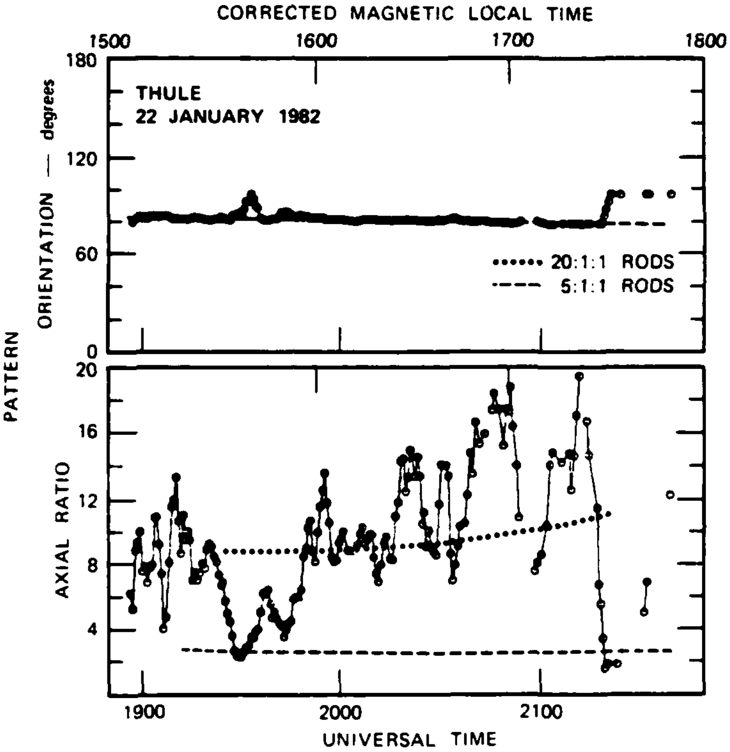

FIGURE 14 LOCAL DUSK-SECTOR DATA

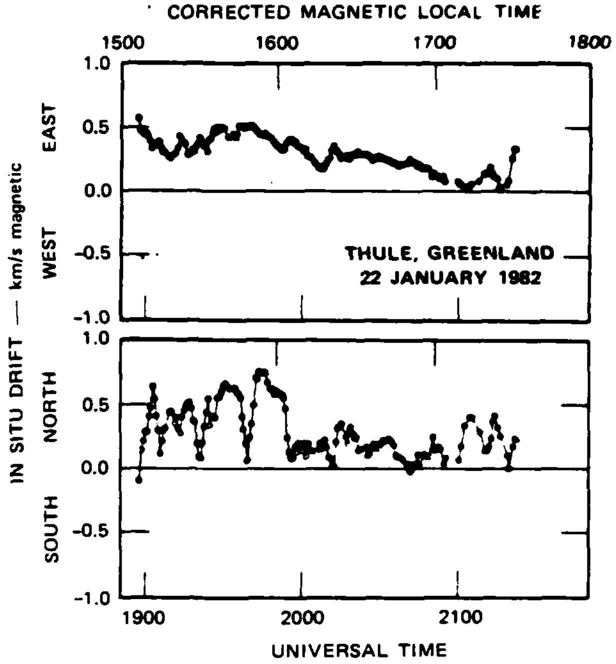

FIGURE 15 LOCAL DUSK-SECTOR DATA

(2) The measured drift patterns in the central polar cap fit the expected two-celled pattern, and can exceed 800 m/s in the dawn, noon, and dusk sectors.

(3) There is a consistent association between drift magnitude and direction, and irregularity anisotropy.

Convection dominance of anisotropy has been clearly demonstrated in the auroral zone, and evidently a similar process is ongoing in the polar cap. The large-scale dynamics of high-latitude fields are relatively well understood and are effectively modeled. If the anisotropy/drift associations can be defined, their definition will greatly simplify global prediction of irregularity occurrence. These associations will be examined directly during joint experiments using the Sondrestrom radar, HILAT, and continued observations of these polar beacons.

In addition to these relatively detailed observations of the irregularity anisotropy and drift and of their interaction, the velocity observations can be combined to yield samples of the large-scale convective flow patterns in the central polar cap. From one day to the next, there are significant changes in the observed flow, both in magnitude and direction. There are major features in the patterns that persist, however, and these are reflected in Figure 16, in which six days of continuous drift measurements have been averaged.

In the figure, the origin of each vector indicates the invariant latitude and corrected MLT of the F-region ray path penetration. As can be seen, these data were taken well into the central polar cap. The satellite orbits change only slightly from day to day, so each vector indicated includes a minimum of ten, and usually more than twenty, individual observations. The velocity magnitudes in the noon sector average 500 to 600 m/s.

There are several features to note in the pattern. First, the flow is generally antisunward in the noon sector, which is expected for the B_Z south IMF sense, which prevailed during these six days. In the dawn and predawn sector, the flow pattern indicates a return to the auroral zone, even at this high latitude. This behavior suggests that the polar cap boundary may be as far north as 80 deg invariant, compared with the average $\sim$ 75 deg boundary seen in the summer [Heppner, 1972]. In contrast to the flows in this sector, which change little from day to day, the dusk drifts are highly variable. Accordingly, the several-day average velocities are reduced in magnitude. The most interesting feature in the pattern, however, is in the premidnight hours near the magnetic pole. The drift in this region is consistently sunward and relatively large.

These are latitudes and times that are not probed from one ground station and a limited number of satellites. We have interpolated the flow into these regions using a simple flow pattern, as indicated by the arrows in Figure 16. The overall picture, then, is one with antisunward flow along a near noon-to-midnight meridian, with direct return to the dawn auroral zone, and a more complex return to the evening auroral zone involving a counterclockwise whorl near the magnetic pole. This is a much more complex pattern than the simple two-celled models [Heelis et al., 1982] of convective flow would suggest. It is, however, very similar to

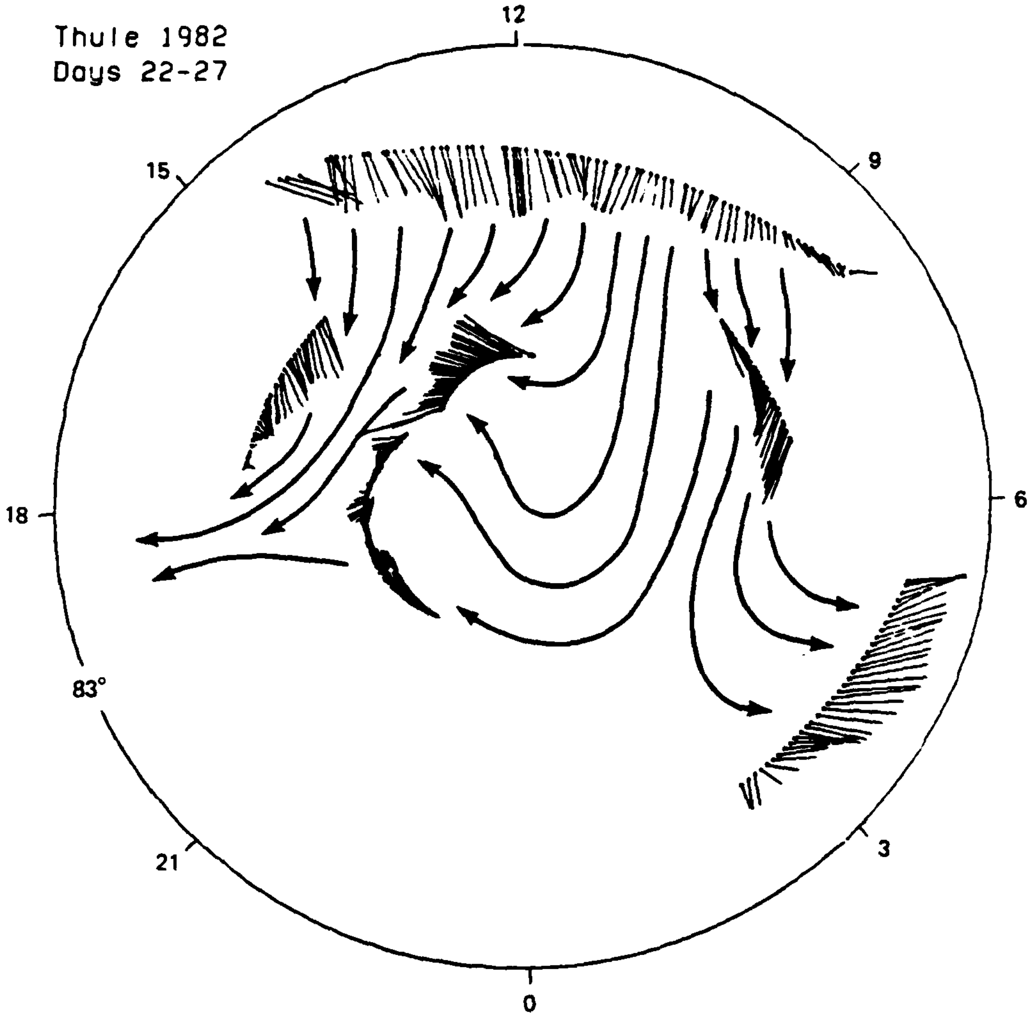

FIGURE 16 AVERAGE FLOW PATTERN IN THE CENTRAL POLAR CAP

one of those systematically observed by the OGO-6 satellite during the summer season [Heppner, 1972].

An advantage of the spaced-receiver scintillation measurements of drift is that the irregularity anisotropy and strength are simultaneously extracted. We are currently studying the morphology of these two parameters within the framework provided by the flow pattern. This study will provide information crucial to the definition of irregularity source regions, decay rates, and structuring mechanisms in the polar cap.

III EQUATORIAL IRREGULARITIES

As was discussed in Section II B, there is still much uncertainty about the role of the E-region conductivity in determining the nature of F-region plasma structure in the auroral zone. On the one hand, a highly conducting E layer damps interchange instabilities by shorting out polarization electric fields; on the other hand, the presence of the E layer may make it possible to tap the magnetospheric free-energy source (that might otherwise be unavailable) via field-aligned currents. Thus, a structured, conducting E layer may provide an additional driver for F-region instability processes.

Although the dynamics of the low-latitude E region are significantly less complicated than those in the auroral zone and are better understood, the role of field-line coupling of the unstable bottomside equatorial F region to the conjugate E layer below is also poorly understood. In the next section we show definitively that the occurrence of E-layer sunset controls the seasonal and longitudinal behavior of spread-F occurrence. Such a relationship had been suggested earlier by Major Wittwer [Private Communication, 1982]. As in the auroral case, the question of whether the control is the result of the removal of a strong damping process or the enhancement of a driving process will await further experiments.

In the latter part of this section, we discuss another "nonlocal" phenomenon in which the E-region plasma, far away from a locally unstable F-region situation, is affected by the F-region instability. We present the first experimental evidence that E-region image striations form in response to the turbulent electric field produced in the unstable F-layer above. Our interest in E-region image striations was prompted by the extensive discussion at the DNA La Jolla conference about the possible role of images in the "freezing" of barium clouds. This freezing effect is the production of a preferred minimum striation scale size. Such freezing might be expected on the basis of numerical simulations [<u>McDonald</u>

et al., 1980]. However, comparisons of barium cloud data with the U-shaped curve [Ossakow et al., 1981] show that the scale size predicted by the curve (using a classic ambipolar diffusion coefficient and the cloud-to-background Pedersen conductivity ratio, m, of the cloud) is too small by approximately a factor of 10 to 30. The scale size predicted by the curve is given by $L = C_m \left[(D_\perp/V)\left((m + 1)^2/(m - 1)\right) \right]$, where $D_\perp$ is the cross-field diffusion coefficient and V is the slip velocity between ions and neutrals.

To make the curve agree with barium cloud observations, we must increase the value of m, or the value of $D_\perp$, or both values. Ossakow et al. [1981] have suggested that m is increased through the formation of E-region image striations. Alternatively, some form of anomalous diffusion may enhance $D_\perp$. We point out below in Section III B that the image formation process itself is highly scale-size selective and produces a favored scale size of $\sim$ 1 km; i.e., very close to the observed freezing scale of barium clouds. This suggests that this process is the key to connecting the freezing scale to the L-shaped curve. However, comparison of more detailed two-level simulations with improved observations is required to settle the issue of whether an increase in m alone is sufficient to explain the freezing effect or whether anomalous diffusion is also important.

A. Control of Equatorial Spread-F by E-Region Conductivity

The occurrence of equatorial scintillations has hitherto revealed a puzzling pattern that appears to vary with both season and longitude [Aarons, 1977; Basu and Basu, 1981]. Scintillation activity has been found to maximize at some observing stations during the equinoctial periods [e.g., Koster, 1972] and at other stations during the local summer [e.g., Livingston, 1980]. This longitudinal variability in seasonal dependence is not strongly controlled by solar activity [Chandra and Rastogi, 1972; Koster, 1972]; that is, the year of observation does not alter the basic seasonal dependence of scintillation activity at a given station [e.g., Rastogi, 1980]. Besides differences in seasonal behavior among observing stations, satellite and multistation observations have revealed distinct longitudinal variations in equatorial irregularity occurrence during a given season [Sharma and Muldrew, 1975; Basu et al., 1976; Aarons et al., 1980; Muldrew, 1980].

Although longitudinal variation in scintillation activity may be expected, for example, because of geomagnetic field variations with longitude [Burke et al., 1980; Maruyama and Matuura, 1980; Abdu et al., 1981], a local seasonal dependence is not. Interpretation in terms of a local seasonal dependence is questionable because the mechanisms believed responsible for the F-region irregularities that produce equatorial scintillations involve entire geomagnetic flux tubes that extend into both conjugate hemispheres [e.g., Tsunoda, 1980; Weber et al., 1983]. Aarons et al. [1980, 1981] attempted to resolve this contradiction by hypothesizing that asymmetric hemispherical variations in F-region plasma density (associated with the equatorial anomaly) might be responsible for the apparent local seasonal dependence. That is, for a given percentage fluctuation, the absolute path-integrated irregularity strength that produces scintillations would be stronger for a higher mean plasma density.

Interpretation of the seasonal and longitudinal dependence of equatorial scintillations should be possible within the framework of existing theories of equatorial irregularity production. The mean behavior of scintillation occurrence (excluding the sporadic day-to-day occurrence pattern) should be amenable to description (and prediction) by the underlying physical processes. There seems little doubt that the occurrence of equatorial scintillations is controlled by the same large-scale processes that control the occurrence of equatorial spread-F (ESF). In other words, the production of irregularities responsible for both equatorial scintillations and ESF is controlled by the effectiveness with which polarization electric fields can develop in the nighttime equatorial F layer. The irregularity production mechanism is believed to be the generalized gradient-drift (or Rayleigh-Taylor) instability. The term "generalized" is used to incorporate, within a single instability description, the different sources of free energy that by themselves are often referred to by various names. Under this term, we include the collisional Rayleigh-Taylor instability driven by gravity [e.g., Dungey, 1956; Haerendel, 1973, Hudson and Kennel, 1975; Scannapieco and Ossakow, 1976], the current-convective instability driven by field-aligned currents [e.g., Ossakow and Chaturvedi, 1979], as well as the ordinary gradient-drift instability driven by neutral winds and electric fields [e.g., Linson and Workman, 1970; Tsunoda, 1981; Tsunoda and White, 1981; Tsunoda et al., 1982].

In this section we compare the occurrence patterns of equatorial scintillations reported in the published literature with the times of sunset in the conjugate E layers, and then show that both the seasonal and longitudinal dependences of scintillation activity are controlled by the rate of change in the integrated E-region Pedersen conductivity. That is, the occurrence maxima in scintillation activity at a given longitude are shown to coincide with times of the year when sunset is simultaneous at the conjugate E layers. We interpret this relationship as support for the concept that equatorial irregularities are produced by the generalized gradient-drift instability, driven by gravity and by field-aligned currents that continue to flow after a rapid decay of the conjugate E layers, as well as by an eastward neutral wind.

1. Observations of Equatorial Scintillations

Observations of equatorial scintillations reported in the published literature are summarized in Table 1. All scintillation statistics, except those presented by Taur [1973], have been reported as percentage occurrence. Taur [1973] tabulated the average monthly number of minutes when scintillations exceeded 0.5 dB, using 6-GHz transmissions from various INTELSAT satellites. Quantitative comparisons among other results (besides those of Taur [1973]) are also difficult because the data were obtained at different frequencies and occurrence statistics were computed using different references. For example, Krishna Moorthy et al. [1978] used scintillations exceeding 0.25 dB at 140 MHz, Paulson [1981] used signal fades greater than 6 dB at 1.54 GHz, and Nichols [1974] used signal fades greater than 5 dB at 254 MHz. The Kwajalein and Ancon results [Livingston, 1980] are based on the scintillation index S4 exceeding 0.6 at 137 MHz. Other factors that would enter into a quantitative comparison are the elevation angle to the satellite and the satellite orbit. Lower elevation angles, of course, would produce more intense scintillations.

Table 1

OBSERVATIONS OF EQUATORIAL SCINTILLATIONS

Author(s)	Place	Frequency	Observations	Maxima
Aarons et al. [1980]	Accra, Ghana	257 MHz	01/77 - 03/78	Feb-Apr
	Huancayo, Peru	257 MHz	01/77 - 03/78	Feb-Apr
	Natal, Brazil	257 MHz	01/77 - 03/78	Nov-Jan
	Guam, U.S.	257 MHz	03/78 - 06/79	Feb-Jul
Bandyopadhyay and Aarons [1970]	Huancayo, Peru	137 MHz	07/67 - 02/69	Sep-Nov
Basu et al. [1980]	Huancayo, Peru	1543 MHz	04/76 - 10/77	Mar,Oct
Chatterjee et al. [1974]	Huancayo, Peru	137 MHz	05/67 - 05/68	Oct-Nov, Mar
Fang and Liu [1982]	Hong Kong, U.K.	4 GHz	01/78 - 06/80	Mar,Sep
Koster [1972]	Legon, Ghana	137 MHz	1967 - 1971	Sep-Oct/ Mar-Apr
Krishna Moorthy et al. [1978]	Trivandrum, India	40, 140, 360 MHz	11/75 - 07/76	Dec,Feb, Jun
Livingston [1980]	Ancon, Peru	VHF-UHF	05/76 - 11/77	Oct-Nov/ Mar-Apr
	Kwajalein, M.I.	VHF-UHF	10/76 - 10/77	May/ Jul-Aug
Nichols [1974]	Kwajalein, M.I.	254.1 MHz	10/70 - 06/72	May,Jul
Paulson [1981]	Guam, U.S.	258/1542 MHz	02/79 - 12/79	Apr,Sep
Taur [1973]	Hong Kong, U.K.	4/6 GHz	08/70 - 11/71	Mar-Apr, Sep
	Guam, U.S.	4/6 GHz	08/70 - 11/71	Apr,Oct
	Tangua, Brazil	4/6 GHz	08/70 - 11/71	Feb-Mar, Oct-Nov
Walker and Chan [1970]	Hong Kong, U.K.	20,40 MHz	10/64 - 07/68	Summer

All satellites except Wideband [Livingston, 1980] were in geosynchronous orbits. Consequently, scintillation occurrence maxima could be determined from continuous measurements. Wideband was in a (sun synchronous) noon-midnight polar orbit, thus limiting scintillation measurements to a narrow local time sector. Fortunately, we are concerned only with the relative occurrence frequency of scintillations, on a monthly basis throughout the year. All geosynchronous satellite results, therefore, can be compared directly; those from the Wideband satellite may require some qualification.

The observations can be categorized into two longitudinal regions, the American-African sector (which includes Huancayo and Ancon, Accra and Legon, Tangua, and Natal) and the Indian-Pacific sector (which includes Trivandrum, Hong Kong, Guam, and Kwajalein). Scintillation observations made at a given longitude were found to have a generally repeatable seasonal dependence; e.g., observations were made from Huancayo (including Ancon) during 1967-69, 1976-77, and 1977-78 showed scintillation activity maxima from February to April, and from September to November. The repeatability of the seasonal dependence in scintillation activity indicates that solar activity is not a major factor.

In the following section, we use the seasonal dependences found by some of the researchers listed above to establish the relationship between scintillation activity and the sunset times at the conjugate E layers. A difficulty with the published results was a tendence for researchers to reduce scintillation occurrence data into three-month averages. Averages over this length of time allow interpretation only in terms of equinox and solstice, and tend to obscure the more subtle relationship between the solar terminator and the geomagnetic flux tubes involved in irregularity generation. Most of our analysis is performed using scintillation activity published as monthly occurrence frequency; however, some of the quarterly averaged results are used in cases where the results from that station were considered important for our purposes.

2. Scintillation Activity and E-Region Sunset

We now examine the seasonal variation in sunset times at the two conjugate E layers for various longitudes. As discussed above, we selected four locations in the American-African sector (Huancayo, Tangua, Natal, Accra) and four in the Indian-Pacific sector (Trivandrum, Hong Kong, Guam, Kwajalein). We investigated the role of E-region sunset in the seasonal occurrence of equatorial scintillations be determining the local solar time (LST) at the dip equator when each of the conjugate E layers enters darkness. For this purpose we used a simplified geometry in which the geomagnetic field line passing over a given observation station is characterized by the geographic latitude at which it crosses the dip equator and the magnetic declination there. The conjugate E layers are then assumed to lie at fixed distances along a great circle path on either side of the dip equator. This geometry is presented in Figure 17 in earth-centered spherical coordinates. The locations of the north geographic pole (N), the dip equator (Q), the subsolar point (S), the conjugate E layers (E, E′), and associated angles are shown.

We are interested in determining the local solar times at the dip equator when the solar zenith angle at each conjugate E layer becomes 90 deg. A nominal solar zenith angle of 90 deg, or ground sunset, was selected because the integrated Pedersen conductivity in the E layer approaches the nighttime value around that time [Baron et al., 1982; Senior, 1980; Vickrey et al., 1981; Watt, 1973]. We first determine the geographic latitude of the E layer by using the law of cosines on triangle NEQ,

$$\theta_E = \sin^{-1}(\sin\theta_Q \cos\ell + \cos\theta_Q \sin\ell \cos D) \quad . \tag{1}$$

The difference in hour angle (or LST) between the dip equator and the E layer is given by

$$\delta = \sin^{-1}(\sin\ell \sin D/\cos\theta_E) \quad . \tag{2}$$

Using Eqs. (1) and (2), we can determine the solar zenith angle at the E layer from the following,

$$\chi_E = \cos^{-1}[\sin\theta_s \sin\theta_E + \cos\theta_s \cos\theta_E \cos(\Delta+\delta)] \quad . \tag{3}$$

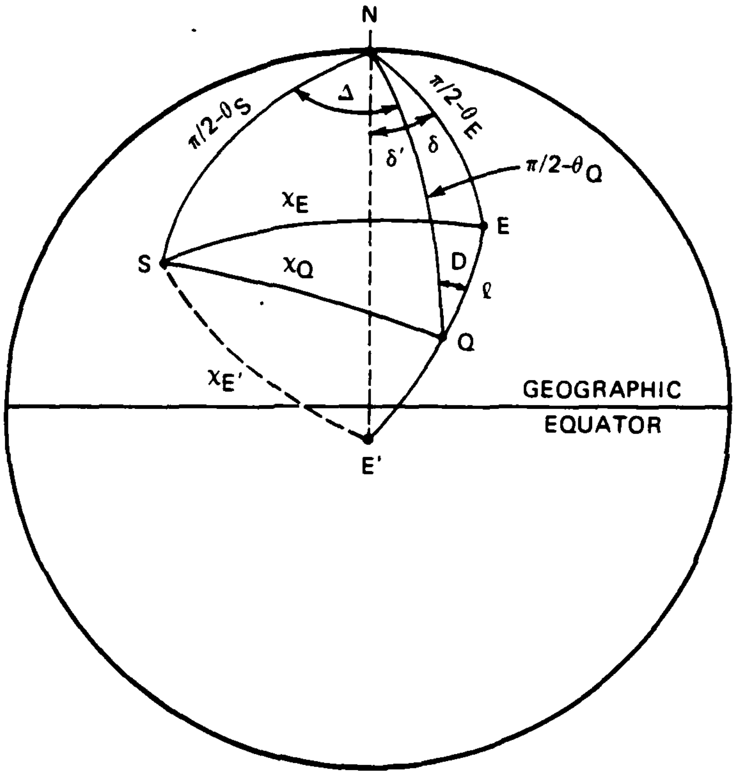

FIGURE 17 EARTH-CENTERED SPHERICAL COORDINATES RELATING THE SOLAR ZENITH ANGLE (χ) AT THE MAGNETIC DIP EQUATOR (Q) AND THE CONJUGATE E LAYERS (E, E') TO THE GEOMAGNETIC FIELD GEOMETRY (D, ℓ)

When the solar zenith angle at the E layer is 90 deg, Eq. (3) reduces to

$$\Delta = \cos^{-1} (-\tan\theta_s \tan\theta_E) - \delta \quad . \tag{4}$$

Equations (1), (2), and (4) are applied to both E layers to determine the seasonal dependence of LST at which the two sunsets occur.

The two features of interest, the seasonal variation of the times when the conjugate E regions enter darkness and the time of year when both E regions enter darkness together, cannot be easily inferred from visual inspection of the above equations. We therefore applied the above equations to the eight selected stations. The characteristics of the geomagnetic field lines passing over the eight stations are listed in Table 2.

Table 2

GEOGRAPHIC AND GEOMAGNETIC PARAMETERS OF STATIONS

Station	Geographic Location (lat,long; in deg)	Dip Equator (lat,long; in deg)	Magnetic Declination (deg)
Accra, Ghana	5.3, -1.1	9.4, -0.7	-7.8
Guam, U.S.	12.4, 147.0	8.0, 144.8	3.2
Hong Kong, U.K.	22.2, 114.2	9.0, 114.3	0.5
Huancayo, Peru	-11.0, -68.5	-12.9, -75.1	2.8
Kwajalein, M.I.	9.4, 167.5	5.8, 166.4	8.8
Natal, Brazil	-5.6, -33.7	-2.8, -37.8	-19.2
Tangua, Brazil	-22.7, -42.8	-8.0, -47.1	-15.0
Trivandrum, India	8.5, 76.9	9.5, 76.7	-2.9

The results for the Indian-Pacific sector are presented in Figure 18, The family of oscillating curves in each panel shows the local times of conjugate E-region sunsets as a function of day of year. Each curve has been labeled with the assumed great-circle ground-distance

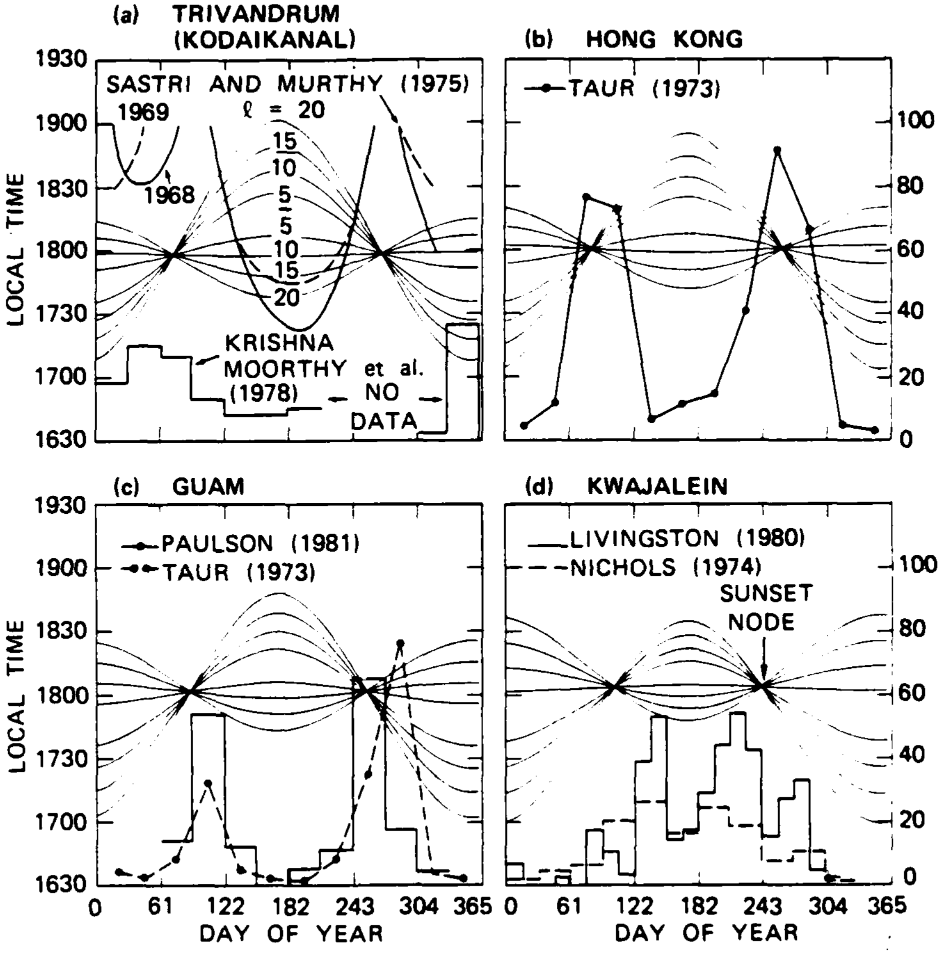

FIGURE 18 COMPARISON OF THE TIMES OF EQUATORIAL SCINTILLATION MAXIMUM TO THOSE OF THE SUNSET NODES, INDIAN-PACIFIC SECTOR

separation of the E regions from the magnetic dip equator. Four E-region spacings (5, 10, 15, 20 deg) were selected to represent expected locations of the magnetic flux tubes filled with scintillation-producing irregularities. All the curves are characterized by two nodes when the local times of E region sunset are identical and by the amplitude of their local-time variation. Of particular interest are the days of the year when the sunset nodes occur. The node spacings in Figures 18(a) through 18(d) are seen to move systematically toward the June solstice, a trend produced by the increasing (eastward) magnetic declination. The maximum peak-to-peak amplitude of the curves, similar for all four stations, is primarily associated with the geographic latitude of the conjugate E regions.

The occurrence frequencies of equatorial scintillations observed at each of the four stations are also plotted with the sunset curves in Figure 18. Referring first to Figure 18(b), we find a simple relationship between E-region sunset times and the occurrence maxima for scintillations; i.e., scintillation activity appears to maximize at times of the year when the sunset nodes occur. Although only the results from Taur [1973] are shown in Figure 18(b), those obtained by Fang and Liu [1982] are nearly identical. Similar results were obtained for Guam, as shown in Figure 18(c). Although the 6-GHz results [Taur, 1973] indicate a displacement between a scintillation occurrence maximum and the fall node, the 1.5-GHz scintillation measurements obtained by Paulson [1981] indicate coincidence.

The Trivandrum results [Krishna Moorthy et al., 1978] shown in Figure 18(a) also indicate a similar relationship between the maxima in scintillation activity and the sunset nodes. The scintillation occurrence is seen to peak around the spring node. No data were available, however, to indicate whether a similar maximum is associated with the fall node. To supplement the scintillation results, we have plotted curves of ESF occurrence at 2100 LST found in ionograms taken at Kodaikanal [Sastri and Murthy, 1975]. During early evening, range-type ESF is known to predominate and to correlate well with the occurrence of scintillations [e.g., Huang, 1970]. The correspondence between ESF occurrence maxima with the two sunset nodes is clear. The only discrepancies appear as a December maximum in scintillation activity and as a January 1968 maximum in ESF occurrence.

Only the Kwajalein results obtained by Livingston [1980] appear to suggest a more complex relationship between sunset nodes and maxima in scintillation occurrence. The results from Nichols [1974] indicate a a broad maximum centered more or less on the June solstice. The broad maximum suggests that conjugate E-region sunsets do not have to occur simultaneously, but that a small but finite time difference may be allowed. The structure in the results obtained by Livingston [1980], however, seems to suggest a close but not coincident relationship between scintillation occurrence maxima and the sunset nodes. The primary occurrence maxima appear to be slightly displaced toward the June solstice; there is even a hint of local minima at the times of the sunset nodes. Recall, however, that these scintillation measurements were made in the midnight sector by a polar-orbiting satellite.

The relationship between seasonal scintillation activity and conjugate E-region sunsets for the four stations in the American-African sector are presented in Figure 19. The Ancon scintillation results [Livingston, 1980], shown as a histogram in Figure 19(a), reveal a coincidence between a maximum in scintillation activity and the spring node. The other scintillation maximum, however, is seen to be shifted away from the fall node toward the December solstice. Scintillation results from Huancayo by Chaturjee et al. [1974] are seen to be in general agreement with the results from the polar-orbiting Wideband satellite. The third scintillation results in Figure 19(a) [Basu et al., 1980] also support the general pattern of the other two curves. The peaks in the third curve, however, indicate a distinct displacement of those peaks away from both nodes toward the December solstice. There appears to be little doubt, therefore, that the displacements are real and repeatable.

The other results presented in Figure 19 appear to be in accord with our finding that peaks in scintillation activity occur during the times of year when sunset is simultaneous at the conjugate E layers. The time coincidence is striking for the Tangua results [Figure 19(b)], although there is a slight displacement of a scintillation maximum away from the spring node towards the June solstice. The comparisons for Natal and Accra also reveal this relationship, despite the fact that three-month

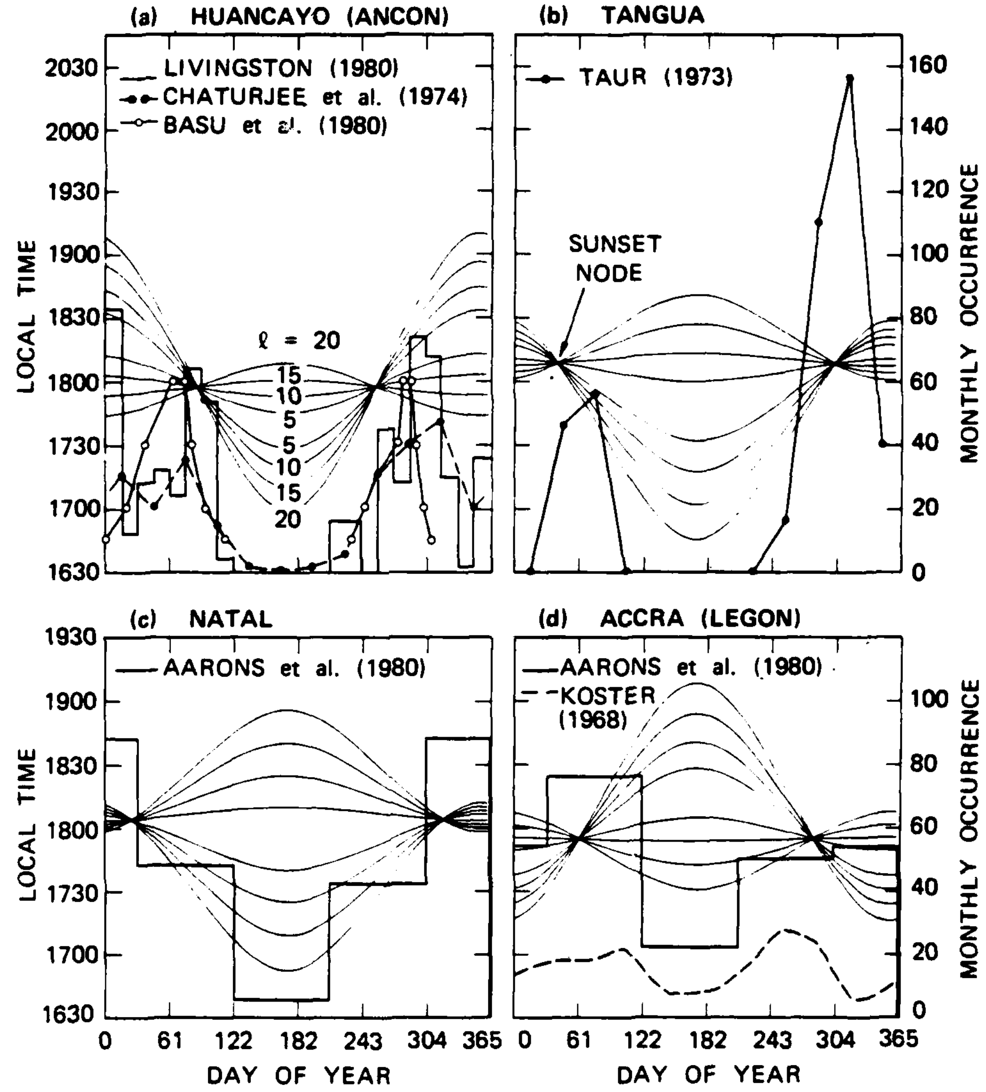

FIGURE 19 COMPARISON OF THE TIMES OF EQUATORIAL SCINTILLATION MAXIMUM TO THOSE OF THE SUNSET NODES, AMERICAN-AFRICAN SECTOR

averaged scintillation results [Aarons et al., 1980] were used. A second scintillation data set, obtained by Koster [1968], also reveals the occurrence of scintillation maxima around the time of the sunset nodes.

A summary of the relationship between scintillation maxima and sunset nodes is presented in Figure 20. We have plotted the months of scintillation maxima and the sunset nodes for each of the eight stations as a function of longitude: Huancayo (H), Tangua (T), Natal (N), and Accra (A), in the American-African sector; and Trivandrum (Tr), Hong Kong (HK), Guam (G), and Kwajalein (K), in the Indian-Pacific sector. In addition, we have supplemented them with equatorial scintillation results [Taur, 1973] from Paumalu, U.S. (P); Lurin, Peru (L); Longovilo, Chile (Lo); Ascension Island, U.K. (As); Ras Abu Jarjur, Bahrain (R); Djatiluhur, Indonesia (D); and Taipei, Republic of China (Ta). At the Indian longitude we have plotted the ESF occurrence results from Kodaikanal [Sastri and Murthy, 1975] instead of the scintillation results from Trivandrum. The longitudinal variations in the months of scintillation maxima, as shown in Figures 18 and 19, are seen to be consistent with those for the sunset nodes.

The monthly trends of the scintillation maxima and sunset nodes may be compared with the longitudinal variations of the magnetic declination and geographic latitude of the dip equator. The gentle convergence of the scintillation maxima and nodes towards the June solstice in the Indian-Pacific sector is seen to be associated with a corresponding slow increase in positive (eastward) declination. A similar variation is seen in the American-African sector where the scintillation maxima (and nodes) move toward the December solstice with increasing negative (westward) declination. The effect of the geographic latitude of the dip equator is best seen in Figures 19(a) and 19(c). The maximum peak-to-peak variation in the time of E-region sunset is seen to be smaller for stations with smaller separations between the dip and geographic equator (Natal) than for stations with larger separations (Huancayo). We see from Figure 19(c) that the scintillation maxima merge into a single broader peak when the nodes are closer together and when the dip equator is close to the geographic equator.

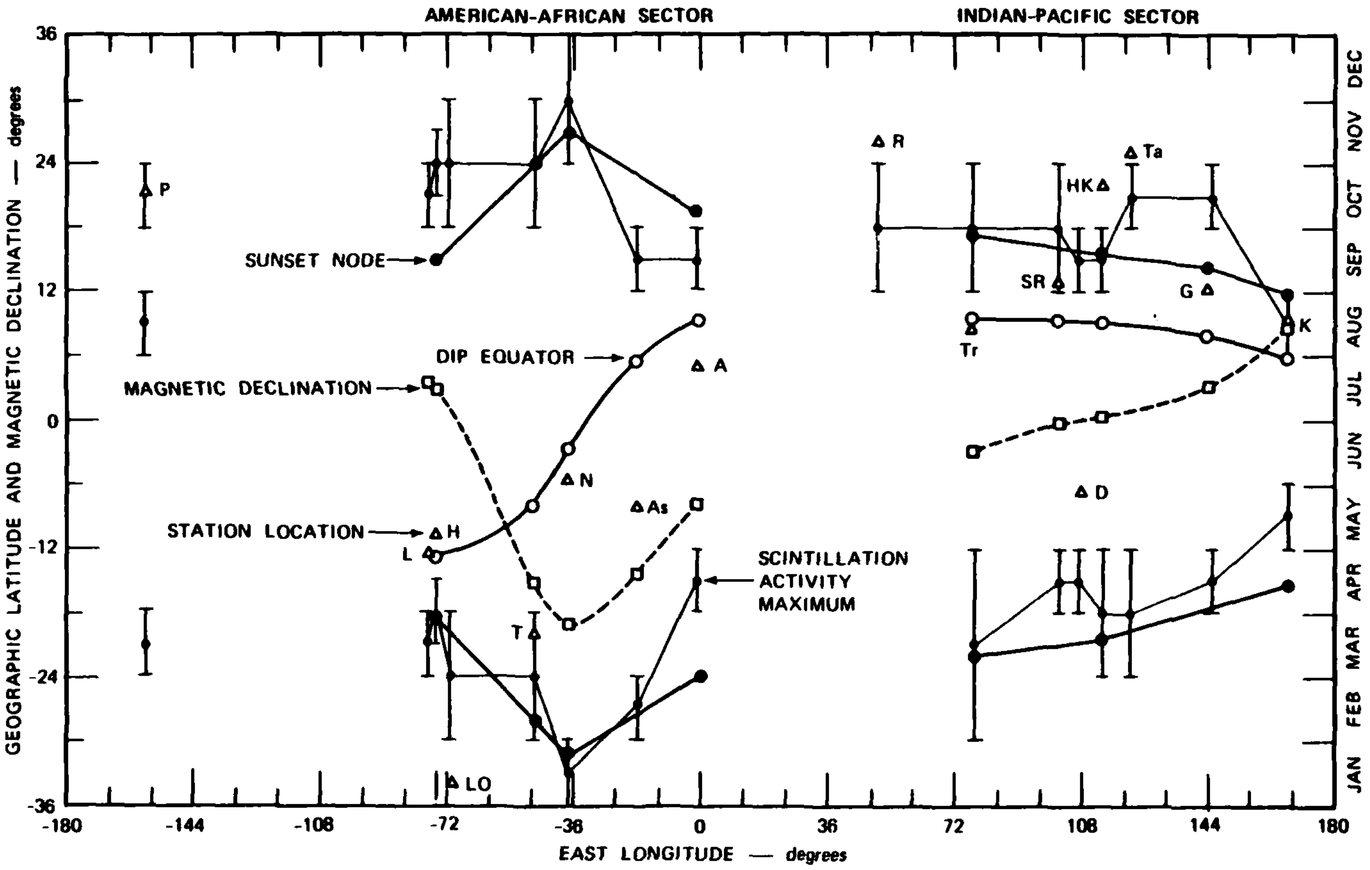

FIGU.RE 20 COMPARISON OF THE LONGITUDINAL VARIATION IN THE TIMES OF SCINTILLATION ACTIVITY MAXIMA AND SUNSET NODES WITH THE MAGNETIC DECLINATION AND GEOGRAPHIC LATITUDE OF THE MAGNETIC DIP EQUATOR

Two features in Figures 18 and 19 suggest other influencing factors besides simple coincidence in sunset times of the conjugate E layers. As mentioned earlier, the primary scintillation maxima were occasionally found to be slightly displaced from one (or both) of the sunset nodes. The second feature is an asymmetry in the occurrence frequency of scintillations. We have found a larger peak associated with the fall node than with the spring node at four stations, Hong Kong, Guam, Tangua, and Huancayo. Paulson [1981] noted the asymmetry in his Guam data and suggested that it might be produced by varying solar activity. We note, however, that Taur [1973] also obtained a similar asymmetry using data taken during different years. A third feature, the isolated occurrence of a scintillation (and ESF) maximum near the December solstice at Ancon (and Kodaikanal), does not appear to be real. The occurrence frequency at Ancon for that time of year was determined from only two satellite passes (the average number of passes is 10) [see Livingston, 1980]. We therefore dismiss that estimate as spurious. Not enough information is available on the Kodaikanal results to assess its validity.

Perhaps the most revealing piece of additional information is the complete absence of scintillation activity at Huancayo during the June solstice when darkness at both E regions occurs at a relatively early local time. In contrast, there is significant scintillation activity at other times of the year when the last sunset at a conjugate E layer is much later than during the June solstice. This finding suggests that simple early unloading of the F-region dynamo [Rishbeth, 1971] is not sufficient reason for enhanced irregularity generation by the generalized gradient-drift instability. As we discuss later in this section, additional (or enhanced) drivers appear to be present during the sunset node period to produce a significantly increased growth rate for the generalized gradient-drift instability.

3. Sunset Nodes and the Longitudinal Conductivity Gradient

Having argued that simple early unloading of the F-region dynamo is not the reason for enhanced irregularity generation, we now suggest that a likely source of free energy is the longitudinal gradient in the integrated E-region Pedersen conductivity. Several researchers, among them Heelis et al. [1974], showed that this conductivity gradient is capable of enhancing the eastward electric field and field-aligned currents, both of which are drivers for the generalized gradient-drift instability. We show that longitudinal gradients are steepest around the times of maxima in scintillation activity.

We begin by deriving formulas for the longitudinal gradient and gradient scale length of the integrated E-region Pedersen conductivity. Senior [1980] showed that the integrated E-region Pedersen conductivity (produced by solar radiation) has the form

$$\Sigma_P = A \cos\chi + B \quad , \tag{5}$$

where χ = solar zenith angle, A = 12, and B = 1 mhos for equinoctial periods. We assume that the total integrated Pedersen conductivity is equal to the sum of the contributions from the conjugate E layers. Using Eqs. (3) and (5), the total integrated E-region Pedersen conductivity is given by

$$\Sigma_P^T = 2B + A \Big\{ \sin\theta_s \, (\sin\theta_E + \sin\theta_{E'}) + \cos\theta_s \, [\cos\theta_E \cos(\Delta+\delta) + \cos\theta_{E'} \cos(\Delta+\delta)] \Big\} \ . \tag{6}$$

Differentiating with respect to longitude yields

$$\frac{d\Sigma_P^T}{d\Delta} = -A \cos\theta_s \, [\cos\theta_E \sin(\Delta + \delta) + \cos\theta_{E'} \sin(\Delta + \delta')] \quad . \tag{7}$$

From our assumption that the integrated conductivities are additive, Eq. (7) shows that the conductivity gradients are also additive. As shown below, sunset at either one of the E layers therefore significantly reduces the longitudinal gradient in integrated Pedersen conductivity.

Using Eqs. (6) and (7), we can also define a gradient scale length,

$$L = \Sigma_P^T \left(\frac{d\Sigma_P^T}{d\Delta} \right)^{-1} \tag{8}$$

Although a gradient scale length does not uniquely characterize the spatial variation in conductivity, we find it useful for qualitative description of the conditions.

To illustrate the behavior of the longitudinal conductivity gradient [given by Eq. (7)] and gradient scale length as a function of time of year, we computed these quantities for $\Delta = 90$ deg, i.e., sunset at the dip equator. We further assumed that the integrated Pedersen conductivity decreased according to Eq. (5) until $\chi = 94.3$ deg when $\Sigma_P = 0.1$ mho, a typical nighttime value [e.g., Harper and Walker, 1977]. From this time on, the darkened E layer is assumed to contribute no longer to the longitudinal gradient or gradient scale length.

The integrated E-region Pedersen conductivity gradient and the gradient scale length for each of the eight selected stations (Figures 19 and 20) are plotted in Figures 21 and 22. For each station we have displayed the gradient scale length in the upper panel and the conductivity gradient in the lower panel. As before, the four curves correspond to specified spacings of the conjugate E layers; the times of the year when the sunset nodes occurred are indicated by vertical lines. The node times can be used to compare these curves to those in Figures 19 and 20.

The gradient scale length curve can generally be described by a sinusoidal variation with a period of one year, interrupted by discontinuous deviations that are dependent on the spacing of the conjugate E layers. The amplitude of the one-year cycle is proportional to the geographic latitude of the dip equator. For example, of the eight stations, the Huancayo curve has the largest amplitude and the Natal curve has the smallest amplitude. The phase of the one-year oscillation is dependent on the hemisphere in which the dip equator is located: those in the

INDIAN-PACIFIC SECTOR

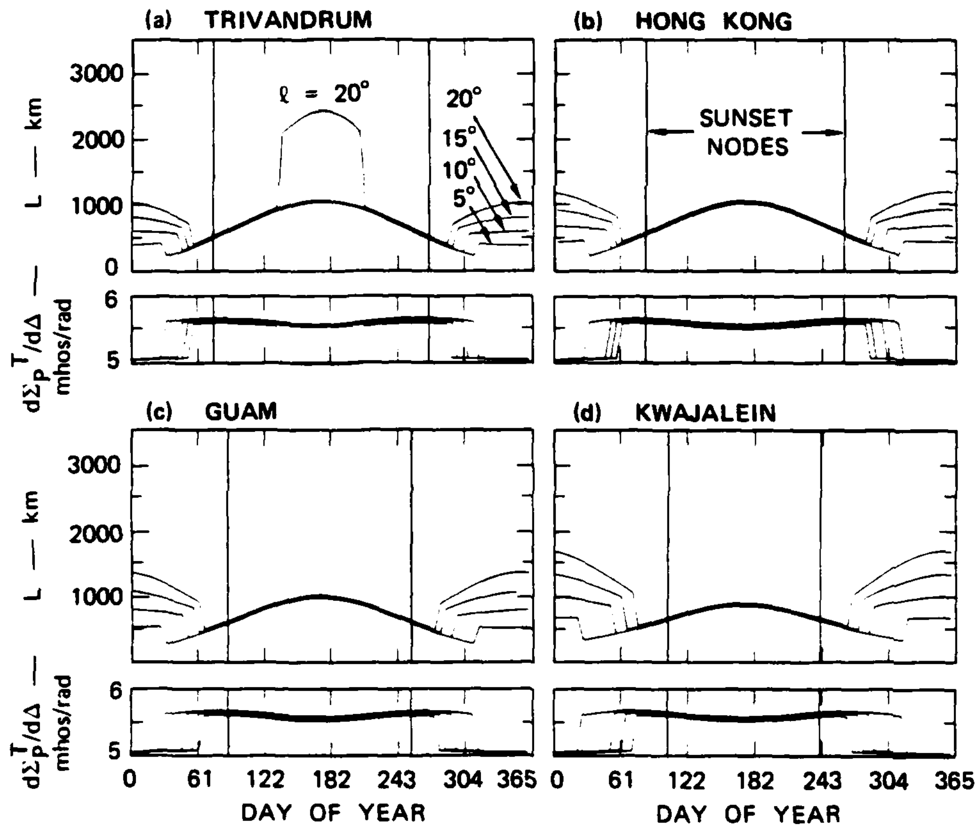

FIGURE 21 THE VARIATION WITH TIME OF YEAR IN THE LONGITUDINAL GRADIENT AND THE GRADIENT SCALE LENGTH ASSOCIATED WITH THE INTEGRATED E-REGION PEDERSEN CONDUCTIVITY, INDIAN-PACIFIC SECTOR

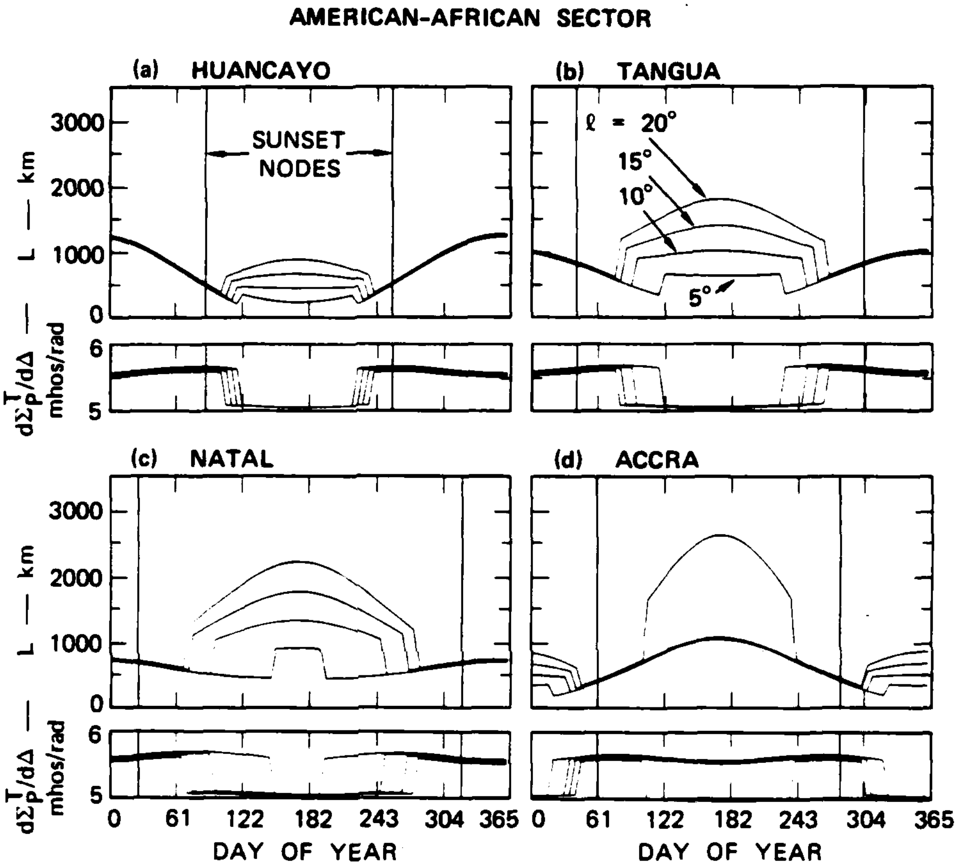

FIGURE 22 THE VARIATION WITH TIME OF YEAR IN THE LONGITUDINAL GRADIENT AND THE GRADIENT SCALE LENGTH ASSOCIATED WITH THE INTEGRATED E-REGION PEDERSEN CONDUCTIVITY, AMERICAN-AFRICAN SECTOR

Southern Hemisphere (Huancayo, Natal, Tangua) have minimum gradient-scale lengths during the June solstice; those in the Northern Hemisphere (Accra, Guam, Hong Kong, Kwajalein, Trivandrum) have minimum during the December solstice.

The discontinuous deviations are produced by the abrupt disappearance of contribution to the gradient scale length by the darkened E layer. When this happens, the gradient scale length increases. The increase is proportional to the spacing of the conjugate E layers and inversely related to the geographic latitude of the dip equator. For example, the increase in gradient scale length is smallest at Huancayo and largest at Natal. Finally, the times of the year when the discontinuities occur are related to the hemisphere in which the dip equator is located. The times of the discontinuities are seen to move toward the December solstice for stations with dip equators in the Southern Hemisphere (Huancayo, Natal, Tangua), and the times of the discontinuities move toward the June solstice for stations with dip equators in the Northern Hemisphere.

The curves for the conductivity gradient are simpler in character than those for the gradient scale length. They are characterized by a semiannual oscillation with amplitude peaks during equinoctial periods and discontinuous decreases produced by sunset at one of the E layers. The semiannual variation in conductivity gradient is small. The seasonal variation in integrated conductivity gradient therefore appears to be controlled by the occurrence of sunset at one of the E layers.

The peaks in scintillation activity, presented in Figures 19 and 20, are found to occur at times of the year when the gradient (gradient scale length) in integrated E-region Pedersen conductivity is steepest (shortest). This conclusion is most convincing if both the gradient and the gradient scale length curves are used. The reader is reminded that the curves in Figures 21 and 22 refer to an arbitrarily selected time (sunset at the dip equator) and are intended to illustrate the qualitative behavior of the longitudinal gradient.

From comparisons of scintillation activity observed at the selected eight stations with sunset times at the conjugate E layers, we have reached the following conclusions:

(1) Peaks in scintillation (and range-type ESF) activity occur during months when sunset is nearly simultaneous at the conjugate E layers.

(2) Although near-simultaneous sunset at conjugate E layers might also be interpreted as the occurrence of earliest total darkness, scintillation activity is not related simply to months of early darkness at both conjugate E layers. The Huancayo results provide the key evidence for this subtle differentiation.

(3) The relationship between scintillation occurrence maxima and sunset nodes is not exact. Slight displacements (up to about a month) in the maxima from the nodes have been found; the displacements, amounting to less than 10 percent, are not necessarily similar for the spring and fall nodes.

(4) The peak value of scintillation activity associated with the fall node has often been found to be larger than that for the spring node. This asymmetry does not appear to be a function of solar activity, as suggested by Paulson [1981].

(5) Peaks in scintillation activity coincide with the times when the longitudinal gradient (gradient scale length) in integrated E-region Pedersen conductivity is steep (short); conversely, there is an absence of scintillation activity when the longitudinal gradient (gradient scale length) is gradual (long). The primary variation in the gradient value is produced by sunset at one of the E layers.

B. Low-Altitude Image Striations Associated with Equatorial Spread-F

Ionospheric plasma instabilities are usually discussed in terms of local parameters. However, as was illustrated in the previous section, because electric fields of scale size $\lambda \gtrsim 1$ km map along magnetic field lines, plasma populations far away from a locally unstable region can affect, and may be affected by, the instability process. Another example is the formation of "image" striations in the E and F_1 regions in response to the electric field produced in the unstable F layer above. The image results principally from a converging velocity field operating on a compressible ion gas. In this section the theory of image formation, including its scale-size dependence, is discussed in detail. Rocket measurements of electron density irregularities are also presented. We show that the spectrum of density structure observed off the magnetic equator is consistent with that expected from the image formation process (which is scale size and density dependent) driven by the gravitational Rayleigh-Taylor instability operating on the bottomside F layer at the equator itself.

As is discussed in more detail below, an image forms at altitudes where the ion gas is compressible, namely, the E and lower F_1 regions. To date such features have not been verified experimentally, although computer simulations have predicted their generation [Goldman et al., 1976; Lloyd and Haerendel, 1973].

The data discussed here come from fixed bias Langmuir probes flown on two rockets launched just off the magnetic equator during equatorial spread-F conditions. The first, a Javalin sounding rocket, was launched by NASA from Natal, Brazil, on 18 November 1973 at 2122 UT [Kelley et al., 1976, 1979; Costa and Kelley, 1978]. The second, a Terrier-Malemute, was launched by the Defense Nuclear Agency from Kwajalein Atoll on 17 July 1979 at 1233 UT [Szuszczewicz et al., 1980; Rino et al., 1981; Kelley et al., 1982]. We will show that the spectrum of density structure observed in the F_1-layer valley (160 to 200 km altitude) off the magnetic equator is consistent with that expected from the image formation process (which is scale length and density dependent) driven by the gravitational Rayleigh-Taylor instability operating on the bottomside F layer at the equator itself.

1. Data Presentation

A plasma density profile from the downleg of the Natal rocket flight is reproduced in Figure 23(a) with an expanded plot of the F-layer valley and E-region density profiles in Figure 23(b). The plasma density profile was extremely structured throughout the flight. Near and just below the F-region peak, the turbulence has been interpreted in

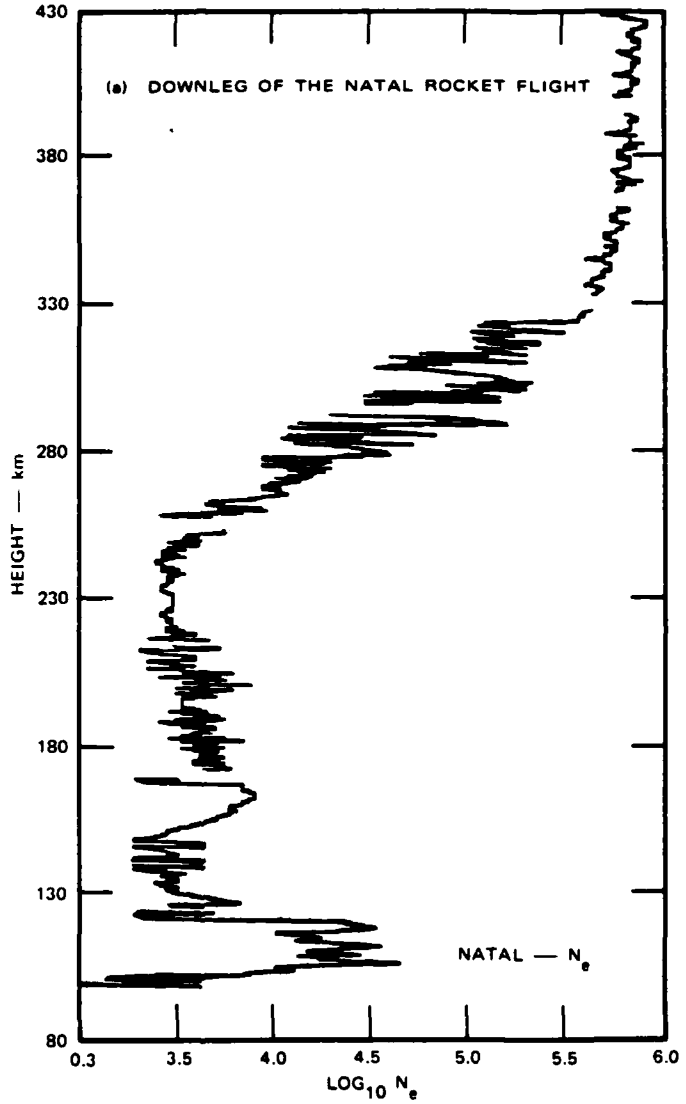

FIGURE 23 EQUATORIAL ELECTRON DENSITY PROFILE

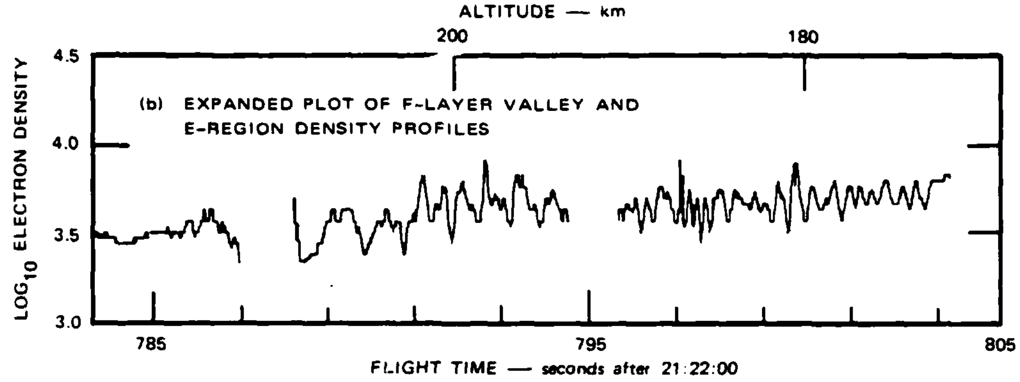

FIGURE 23 (Concluded)

terms of the non-linear gravitational Rayleigh-Taylor instability (see earlier references). The low-altitude (90 to 130 km) structure is the result of classic sporadic E layers and is not produced by the "image" process. Of interest to the present study are the quasi-sinusoidal fluctuations in the F_1-layer valley (170 to 200 km), where the zero-order vertical plasma density gradient nearly vanishes. Because of the finite dip angle at Natal, these fluctuations project along magnetic field lines to the magnetic equator at heights ranging from 280 to 315 km. Note that this altitude range corresponds to heights where the local equatorial F region was observed to be unstable to the gravitational Rayleigh-Taylor process. The geometry is illustrated schematically in Figure 24.

Another example from the Plumex rocket downleg is presented in Figure 25. Again, quasi-sinusoidal oscillations were observed in the F_1-layer valley region at heights that map to the magnetic equator in the region where local equatorial spread-F was detected. Conversely, the electron density profiles reported by Morse et al., [1977] and Mr. S. Prakash [private communication, 1982], which were obtained very near the dip equator in Peru and India, respectively, showed no such structure in the F_1-layer valley. Thus, in all, five equatorial rocket flights have shown E-region structure or the lack thereof in a manner consistent with low-altitude structure being formed by the image process.

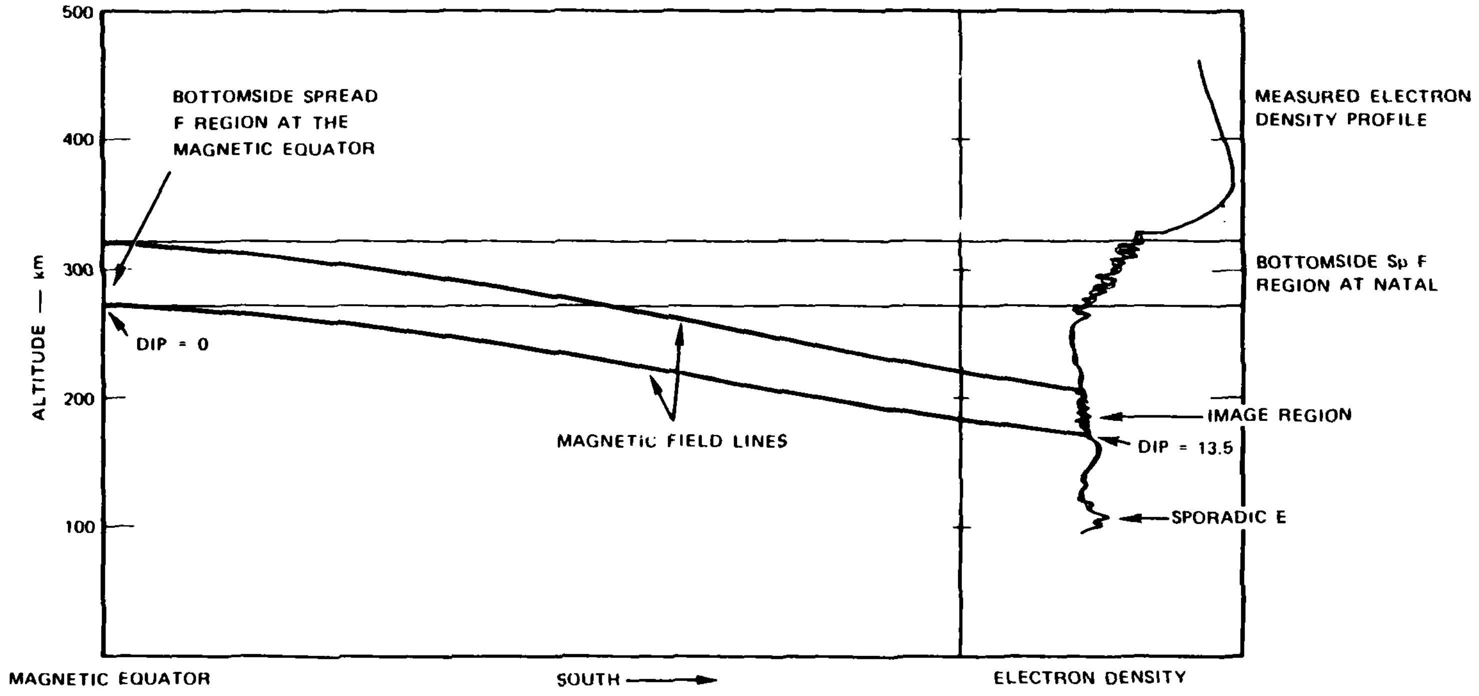

FIGURE 24 SCHEMATIC DIAGRAM OF THE MAGNETIC FIELD GEOMETRY

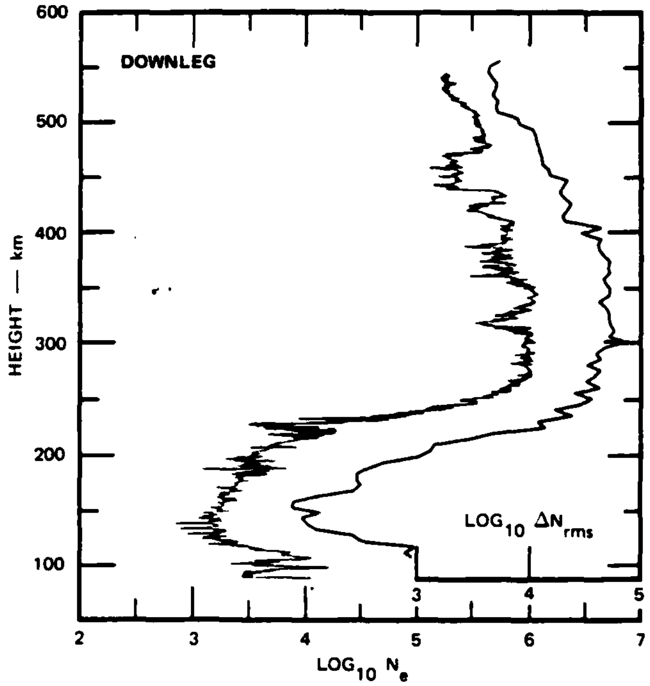

FIGURE 25 PLUMEX ROCKET DOWNLEG

A series of spectra corresponding to different altitude ranges from Figure 23 are presented in Figures 26 and 27. The Figure 26 spectra all correspond to bottomside equatorial spread-F. The spectrum from the lowest altitude displays a form that varies at k^{-2} over the regime from λ = 5000 m to λ = 50 m, where the instrument noise level was reached. The highest altitude spectrum seems to have a somewhat shallower spectral form at the long wavelengths (500 to 5000 m). These results are in good agreement with the Plumex I results reported by Rino et al., [1981], and Kelley et al. [1982].

The F_1-layer valley spectra in Figure 27 are quite different from those in Figure 26, as are the waveforms. The spectra are peaked between 2 to 3 Hz, which corresponds to wavelengths of 700 to 1400 m. The peaked spectra are consistent with the quasi-sinusoidal nature of the waveforms. We show in the next section that such a peaked spectra should be expected on the basis of the image formation process.

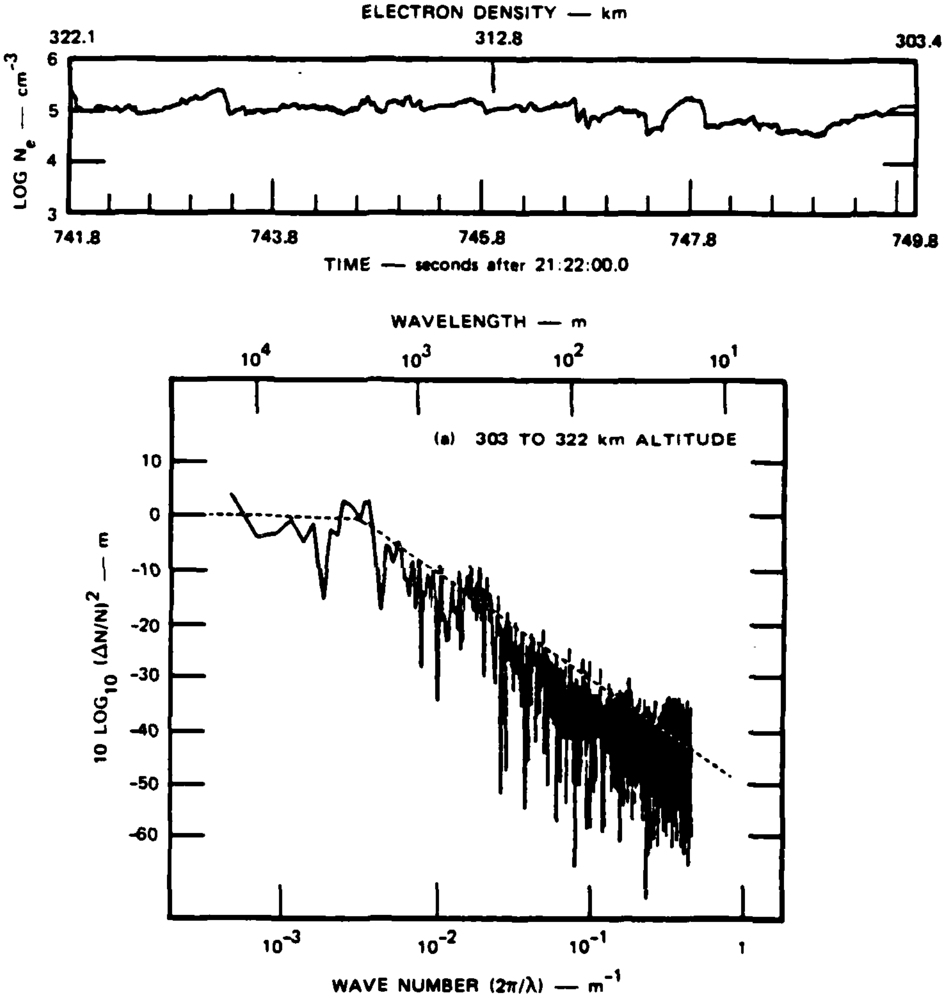

FIGURE 26 A SERIES OF SPECTRA CORRESPONDING TO DIFFERENT ALTITUDE RANGES FROM FIGURE 25

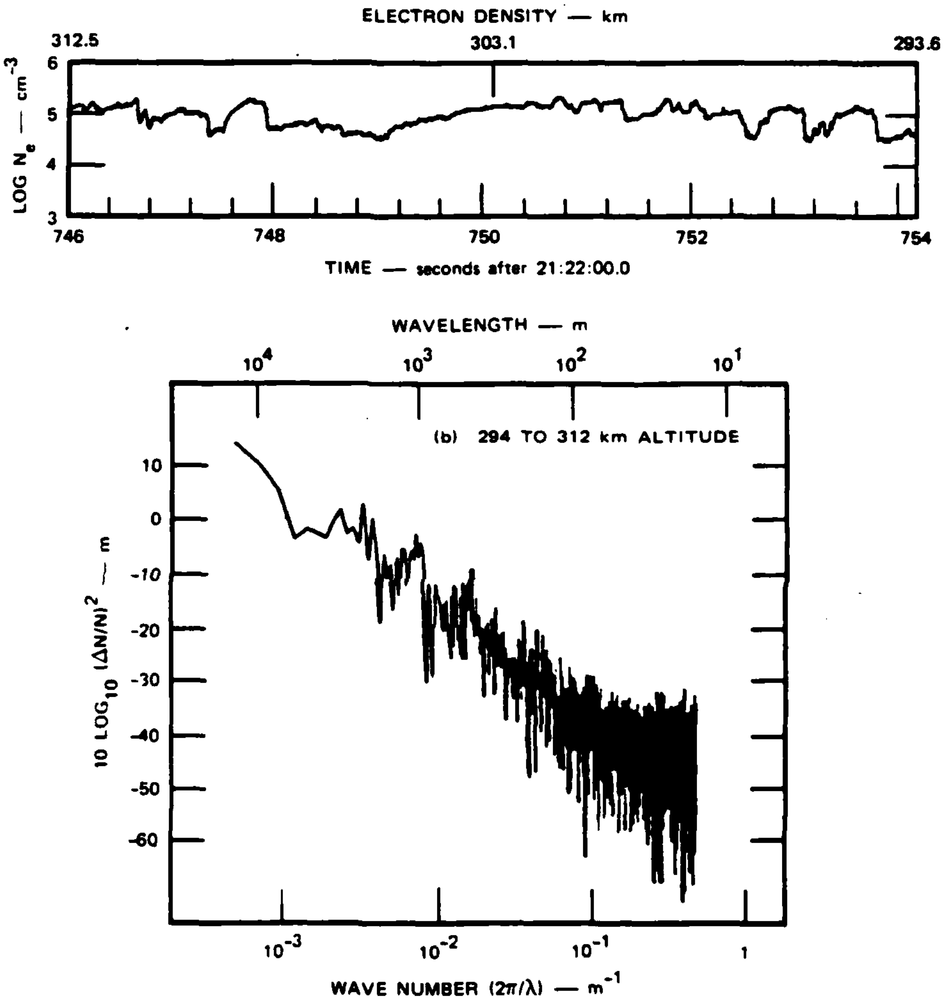

FIGURE 26 (Continued)

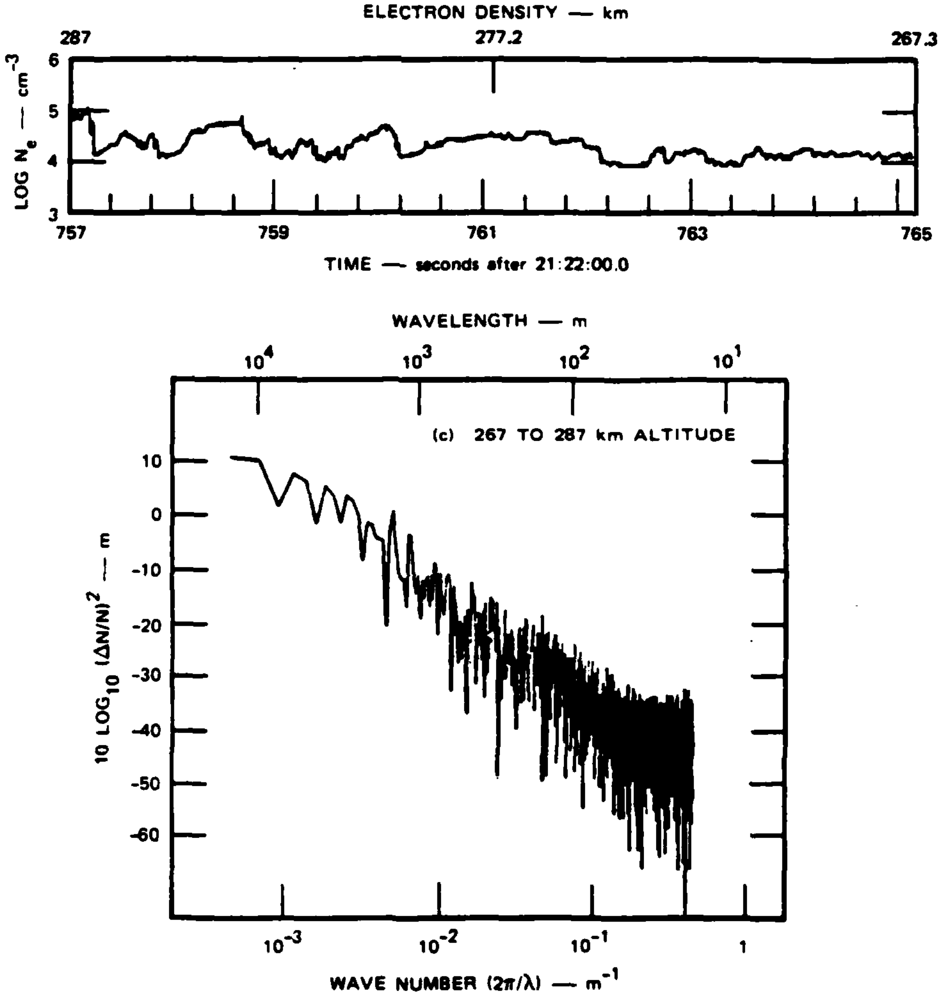

FIGURE 26 (Concluded)

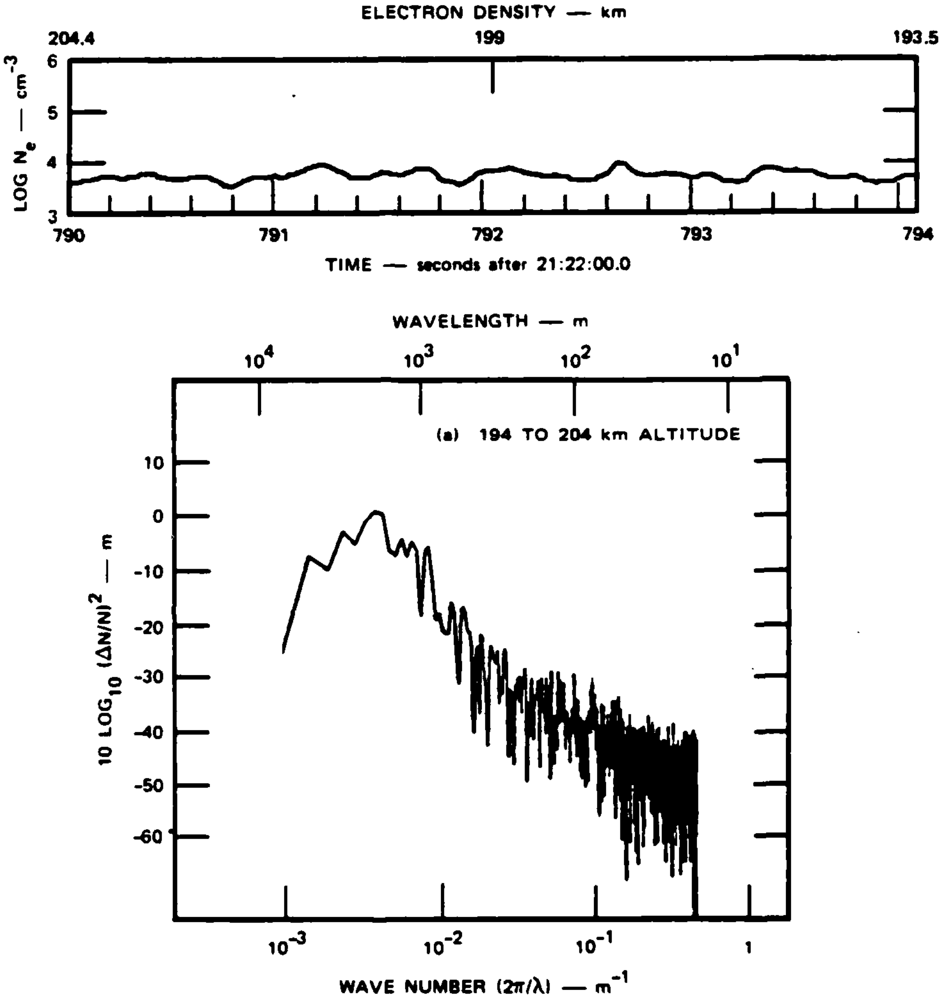

FIGURE 27 A SERIES OF SPECTRA CORRESPONDING TO DIFFERENT ALTITUDE RANGES FROM FIGURE 25

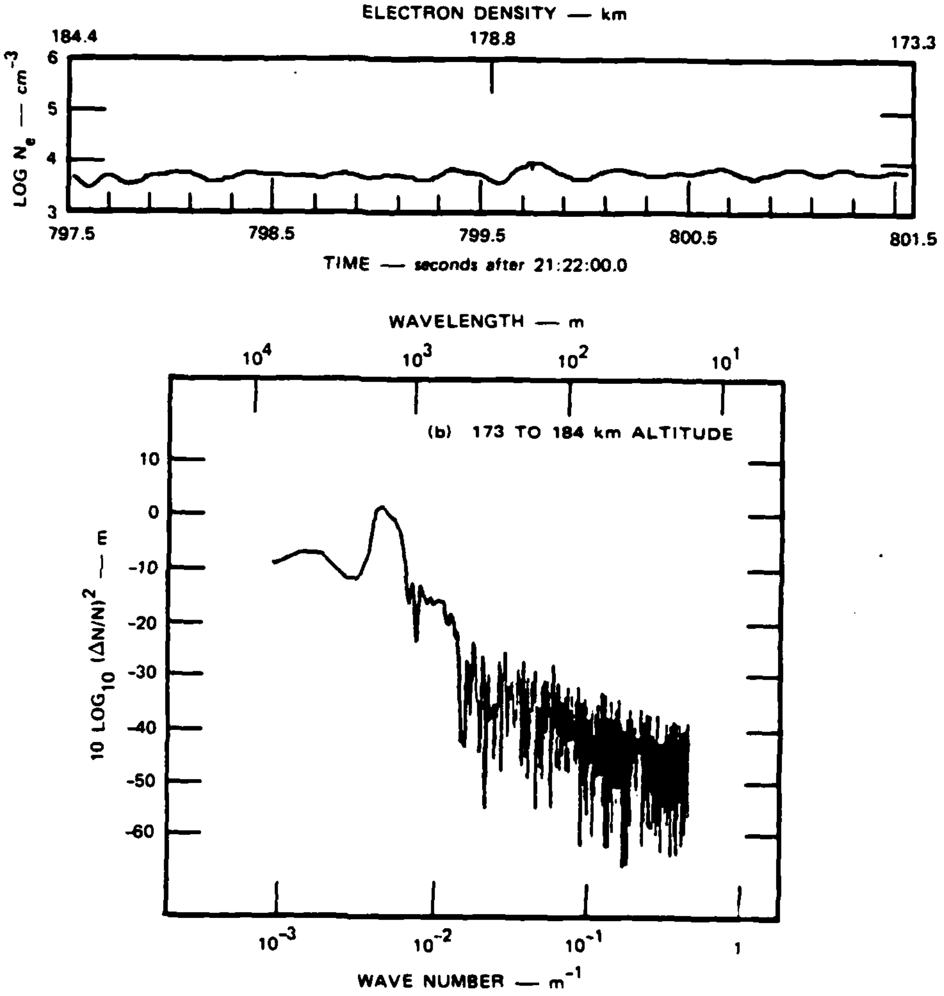

FIGURE 27 (Concluded)

2. Analysis

The mechanisms whereby plasma irregularities are formed in the F layer ionosphere can be studied by considering the continuity equation:

$$\frac{\partial n^F}{\partial n} + \underset{\sim}{\nabla} \cdot (n^F \underset{\sim}{v}) = P - L \quad , \qquad (9)$$

where n is the electron density, $\underset{\sim}{v}$ is the flow velocity, P the production rate, and L the loss rate. In the nighttime F layer the latter two terms can be ignored, yielding

$$\frac{\partial n^F}{\partial t} + \underset{\sim}{V} \cdot \underline{\nabla} n^F + n^F(\underset{\sim}{\nabla} \cdot \underset{\sim}{v}) = 0 \quad . \qquad (10)$$

Ignoring variations along the direction of the magnetic field, the primary velocity is given by $\underline{E} \times \underline{B}/B^2$, which is divergence free, and thus

$$\frac{\partial n^F}{\partial n} = - \underline{V} \cdot \underline{\nabla} n \quad . \qquad (11)$$

In effect, the irregularities are formed by incompressibly mixing an existing background density gradient via the perturbation electric fields generated in the instability process. These processes are reasonably well understood and well documented (see recent reviews by Fejer and Kelley [1980] and Ossakow [1981]). For our purposes here, we need only describe the perturbation electric field (or equivalent velocity) structure in the unstable F layer because it is this structure that maps to lower altitudes and drives the image process.

It can be shown from nonlinear Rayleigh-Taylor instability theory with no zero-order zonal electric field [Keskinen and Ossakow, 1981], that the electric field and density fluctuations are related by:

$$\delta E = \frac{gB}{\nu_{in}^{F}} \left[\frac{\delta n}{n}\right]^{F} \quad , \tag{12}$$

where g is gravitational acceleration, B is the magnetic field strength, ν_{in}^{F} is the ion-neutral collision frequency, and $\left[\frac{\delta n}{n}\right]^{F}$ are density fluctuations like those whose spectra are shown in Figure 26. Thus, the velocity turbulence driving image formation can be easily specified in terms of our measurements of the density fluctuations. Our goal then is to show that the spectrum of image irregularities observed is the result of a balance between this scale-size-dependent driver and the image formation and diffusive damping processes that are also scale-size dependent. Equation (12) also applies to midlatitude barium clouds if $\left(g/\nu_{in}^{F}\right)$ is replaced by (E'/B), where E' is the electric field measured in the neutral frame of reference.

Note that the Rayleigh-Taylor process will not create structure in the F-layer valley if the zero-order density gradient vanishes. The electric field would still map to the region where density structure is observed, but with no density gradient the stirring will not produce structured density.

To understand the formation of images, we must examine a more complicated version of the continuity equation. As will be discussed in more detail below, images form at altitudes where the incompressibility assumption used in the previous discussion breaks down. Compressibility arises from nonnegligible Pedersen drifts $\left(V_P = \frac{\sigma_P}{nq} E\right)$ that must be added to the $\bar{E} \times \bar{B}$ flow considered above. Here σ_P is the Pedersen conductivity, which for E- and F_1-layer heights is given by

$$\sigma_P = \frac{nq^2 \, \nu_{in}^{E}}{m_i \, \Omega_i^2} \tag{13}$$

where q is the electron charge, m_i and Ω_i are the ion mass and gyrofrequency, respectively, and ν_{in}^E is the ion neutral collision frequency at the image altitude. Throughout what follows, the superscript E will denote quantities at the image altitude even though we are concentrating principally on the F_1-layer valley region. Additional complications to the continuity equation include the effects of relatively rapid cross-field plasma diffusion and chemical recombination. If we include these effects, Eq. (10) becomes

$$\frac{\partial n^E}{\partial t} + \frac{q}{\nu_{in}^F} + \frac{\bar{E} \times \bar{B}}{B^2} \cdot \nabla_Z n^E - n_o^E \frac{q\nu_{in}^E}{m_i\Omega_i^{E2}} \nabla \cdot \bar{E} - D_\perp \nabla_\perp^2 n^E - \alpha n_o^{E^2} = 0 \quad , \qquad (14)$$

where we have ignored any horizontal variation in electron density but have, for completeness, included a vertical gradient term that is weak in the valley region. $D_\perp$ is the cross-field plasma diffusion rate, and α is the effective recombination coefficient. Dividing through by n_o^E, we obtain an expression for the linear growth rate of the image striation, $\gamma_{image} = \frac{1}{n_o^E}\frac{\partial n^E}{\partial t}$.

$$\gamma_{image} = \left(\frac{\bar{q}}{\nu_{in}^E} + \frac{\bar{E} \times \bar{B}}{B^2}\right) \cdot \frac{\nabla_Z n^E}{n_o^E} + \frac{q\nu_{in}^E}{m_i\Omega_i^{E2}} \nabla_\perp \cdot \bar{E} - D_\perp \nabla_\perp \cdot \left(\frac{\nabla_\perp n^E}{n_o^E}\right) - \alpha n_o^E \qquad [15(a)]$$

Thus, growth of images will occur if

$$\gamma_{image} = \gamma_{stir} + \gamma_{conv} - \gamma_{diff} - \gamma_{chem} > 0 \quad . \qquad [15(b)]$$

Before discussing the physical significance of each of the terms, we should recall that the electric field, $\bar{E}$, is the perturbation electric field associated with the driving instability operating on the bottomside F layer and mapped to the lower altitude image region. For the electric field fluctuations to map, they must be of scale sizes larger than several hundred meters [Farley, 1959, 1960]. Also, for the steady state conditions considered here, images must form at the same scale size as the driving F-layer instability striations [see Vickrey and Kelley, 1982]. An additional subtlety of Eqs. (13) and [15(a)] is that we have assumed $D_\perp$ in the diffusion term, γ_{diff}, to be independent of density so that we could bring it outside the divergence operator In reality, $D_\perp$ depends on electron density through electron-ion collisions, but at the altitudes of present interest this dependence is negligible compared with the dependence on ion-neutral collisions.

The physical processes that compete to determine whether an image forms at a given scale size and background density may be described as follows. The stirring term γ_{stir} in Eq. [15(b)] can produce an image if plasma of different densities (from different heights in the equatorial situation) is mixed on a time scale that is short compared with the time it takes for the plasma to recombine or diffuse away. This time scale is determined by the magnitude of the mixing velocity and the steepness of the density gradient. In the present situation, the density gradient of interest is the vertical scale height at the image altitude. However, because this scale height L_v was so large in the present case [$L_v \sim 60$ km in Figure 22(a)], this term is important only at very large scales. It may be noteworthy for other situations, however, that the scale-size dependence of γ_{stir} is the same as that of the driving velocity fluctuations in the unstable F layer.

The second term in Eq. [15(b)], γ_{conv}, represents the formation of an image caused by a converging velocity field operating on the compressible ion gas. The electron gas is still incompressible at image altitudes, and thus electrons must flow up and down along magnetic field lines to maintain charge balance [see discussion by Vickrey and Kelley, 1982a]. Note that the divergence operator introduces an additional scale-size dependence to the γ_{conv} term. Small-scale fluctuations in the velocity field form images more readily than do large-scale fluctuations of the same magnitude [Vickrey and Kelley, 1982a]. As was the case with the stirring term, however, the convergence of plasma must proceed at a rate faster than its recombination rate in order for an image to form. Thus, as the background density is increased, smaller scale image growth will be favored.

The term γ_{chem} in Eq. [15(b)] represents chemical recombination of the image region plasma. At altitudes where the ion gas is compressible, the ionospheric ion composition tends to be dominated by molecular ions (i.e., NO^+ and O_2^+). The recombination rate for these species varies as αn^{E^2}, which produces a strong density dependence in contrast to the F-layer plasma where the driving instability operates. At F-layer heights the recombination rate of O^+ is proportional to n^F instead of n^{F^2}. Hence, the time constant for recombination, $\frac{1}{n_o^F}\frac{\partial n^F}{\partial t}$, is independent of electron density.

Now let us examine the scale-length dependence of the image growth rate expression. Making use of Eq. (12) we can Fourier Transform Equation [15(a)] to obtain

$$\gamma_{image}(k_o) = \left[\frac{1}{L_v}\left(\frac{g}{\nu_{in}^F} + \frac{g}{\nu_{in}^E}\right) + \frac{\nu_{in}^E}{\Omega_i}\left(\frac{g}{\nu_{in}^F}\right)k_o\right]\left[\int_{k_o-\Delta k/2}^{k_o+\Delta k/2} P^2(k)\,dk\right]^{\frac{1}{2}}$$

$$- k_o^2 D_\perp - 2\alpha n_o \tag{16}$$

where $P(k) = \frac{\delta n^F}{n_o^F}(k)$. The spectra in Figure 25 are well represented by

$$P^2(k) = \frac{1}{1 + \left(\frac{k}{k_c}\right)^2}\,(m) = \frac{1}{1 + 2.6 \times 10^4 k^2}\ , \tag{17}$$

corresponding to $k_c = 6.2 \times 10^{-3} m^{-1}$.

Figure 28 shows plots of $\gamma_{image}(k)$ versus k for typical F-layer valley conditions corresponding to the observations discussed above, i.e., $\nu^E_{in}/\Omega_i = 0.1$, $g/\nu^F_{in} = 100\ m\ s^{-1}$, $D_\perp = 10\ m^2\ s^{-1}$, and $\alpha = 5 \times 10^{-8} cm^3 s^{-1}$ [Vickrey et al., 1982]. It is important to point out that the detailed shape of the curve and the magnitude of $\gamma(k)$ depend on the choice of the integration interval Δk in Eq. (16). To produce the curves we have chosen values of Δk that are roughly equal to the bandwidth of the observed irregularity spectrum. This interval represents a "bandpass" of driving fluctuation wavenumbers about the image scale size of interest. Because the choice of integration interval is arbitrary, one must not attach too much significance to the magnitude of the growth rates in Figure 28. Nonetheless, the theoretical prediction of a narrow band of preferred image scale size is very significant. A comparison of the curves labeled (a) and (b) in Figure 28 illustrates the effect of doubling the integration interval Δk. As one would expect, the growth rate increases for all scales with the integration interval Also, the most preferred value of k increases, but only by about 20 percent. Thus, the prediction of a preferred scale is not highly sensitive to the integration interval chosen.

The scale-size dependence of the image growth rate also depends, of course, on the irregularity spectrum of bottomside spread-F, $P^2(k)$, which is assumed to drive the image process. To examine the sensitivity of $\gamma_{image}(k)$ to the assumed spectral shape, we have halved and doubled the value of k_c in Eq. (17) to construct curves (c) and (d) in Figure 28. The integration interval was the same as that for curve (a). As can be seen in the figure, even these rather dramatic changes in the driving spectral characteristics do not drastically change the preferred scale size produced. Our best estimate of the conditions appropriate to the observations presented above corresponds to curve (a), which predicts a preferred image scale of $\sim$ 750 m. This prediction is in good agreement with the preferred irregularity scale sizes shown in Figure 27. One must keep in mind, however, that although a peaked growth rate is conceptually pleasing in a process that ultimately results in a narrow spectrum of density irregularities, there is no fundamental reason why the fully developed (nonlinear) density spectrum should necessarily match the linear growth rate exactly.

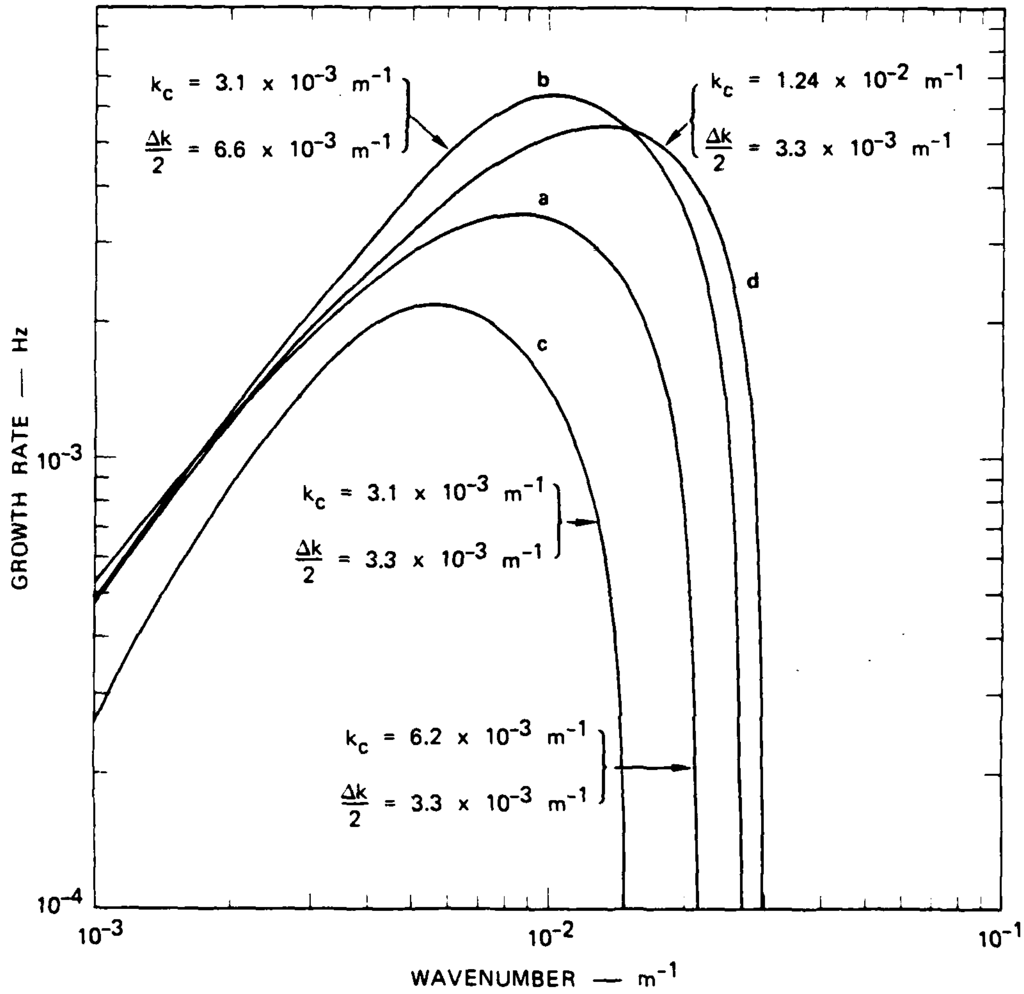

FIGURE 28 WAVELENGTH DEPENDENCE OF THE IMAGE GROWTH RATE FOR F_1-REGION VALLEY ALTITUDES. The various curves illustrate the sensitivity of the results to changes in the integration interval Δ/k and driving spectrum P(k).

To determine whether the magnitude of the predicted image growth rates is significant, we can compare it with the linear growth rate of the driving process, γ_{RT}.

$$R = \frac{\gamma_{conv}}{\gamma_{RT}} = \frac{k_o \left(\frac{\nu_{in}^E}{\Omega_i}\right)\left(\frac{g}{\nu_{in}^F}\right)\left(\frac{\delta n}{n}\right) \Delta k}{\left(\frac{g}{\nu_{in}^F}\right)\left(\frac{1}{L_F}\right)} , \tag{18}$$

where L_F is the zero-order vertical gradient on the bottomside of the F layer, and

$$\left(\frac{\delta n}{n}\right) \Delta k = \left[\int_{k_o - \Delta k/2}^{k_o + \Delta k/2} P^2(k) dk \right]^{\frac{1}{2}} . \tag{19}$$

Since $\left(\frac{\delta n}{n}\right) \Delta k$ is about 5 percent in the bandpass interval of the observed images, $(\nu_{in}^E/\Omega_i) \sim 0.1$, $L_F \sim 20$ km, and the value of k_o at the peak of the image growth rate is $\sim 10^{-2} m^{-1}$, then $R \approx 1$. Thus, the growth of images should occur on a similar time scale to that of the "parent" striations. We show below that γ_{image} is even faster at lower altitudes for comparable electron densities. Thus, since the occurrence of bottomside spread-F is well known and documented, the formation of image striations should not be too surprising.

Although we have no direct observations of image formation in the E region, the process should proceed more rapidly there (provided the density is low enough, e.g., Vickrey and Kelley, 1982a) because the ion gas is more compressible at E-region heights than at F-region heights. In Figure 29 we have calculated the image growth rate $\gamma_{image}(k)$ for E-region conditions; i.e., $\nu_{in}/\Omega_i = 1$, $D_\perp = 100 \ m^2 s^{-1}$, and $\alpha = 2 \times 10^{-7} cm^{-3} s^{-1}$

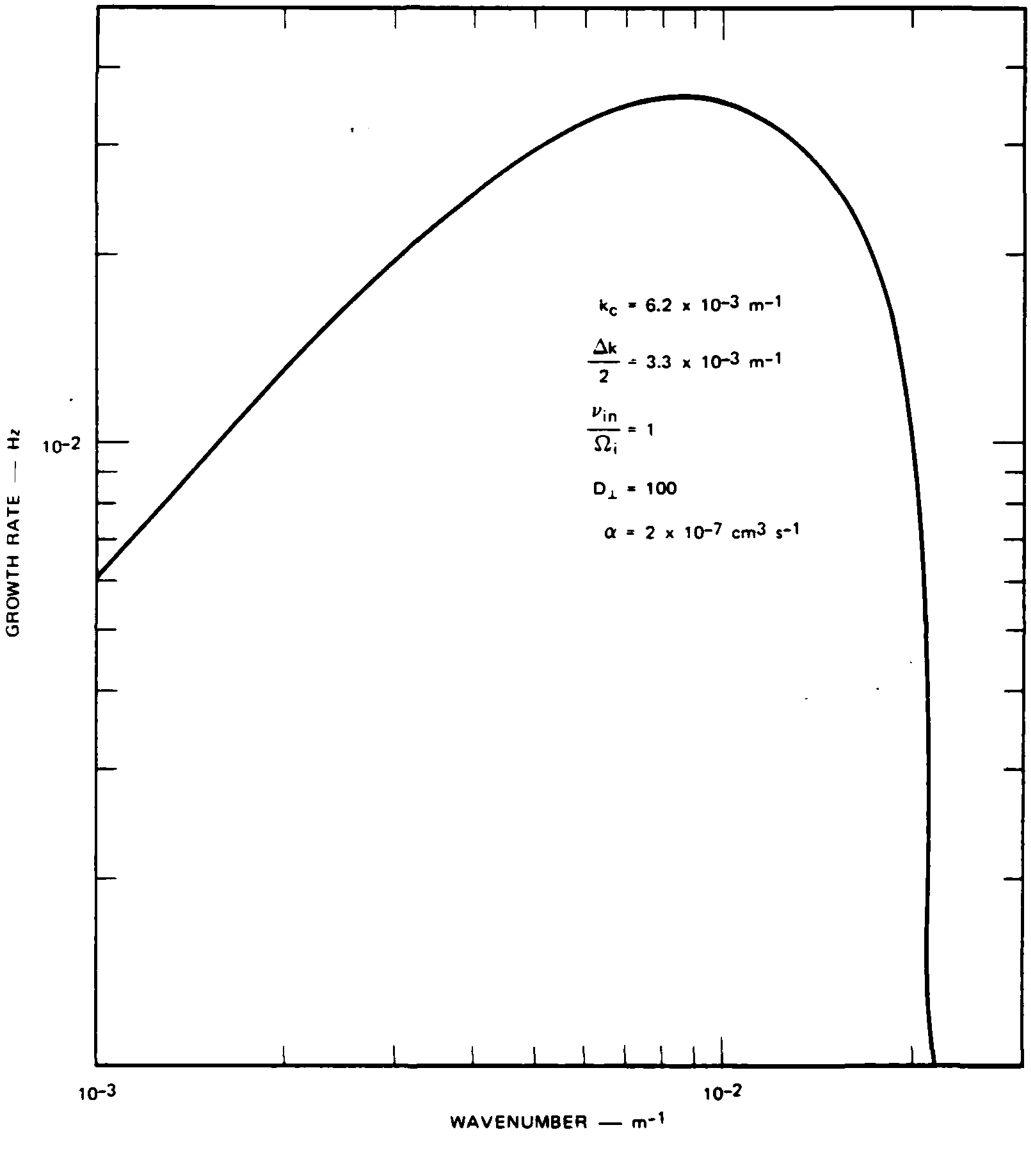

FIGURE 29 WAVELENGTH DEPENDENCE OF THE IMAGE GROWTH RATE FOR E-REGION ALTITUDES

[Vickrey et al., 1982]. The integration interval and k_c are the same as Figure 28 curve (a). We find, as at higher altitudes, a preferred image scale size of $\sim$ 700 m is produced. In this case, however, the image growth rate is approximately two orders of magnitude faster than at F_1-layer altitudes provided the electron density is comparable.

We have presented here what we believe to be the first direct evidence for the formation of image irregularities in the ionospheric medium. We have also computed a linear growth rate for the structures and find that the k dependence matches the observed spectrum quite well.

The case we have studied involves images of F-region irregularities created by the Rayleigh-Taylor process in equatorial spread-F. A similar analysis should apply, however, to midlatitude barium cloud striations that should also create E-region images in the same scale-size regime as presented here. For example, Kelley et al. [1979] showed that power spectral measurements in a striated barium cloud matched quite closely the bottomside spread-F spectrum measured in the Natal flight discussed here in both absolute magnitude and scale size. Thus, E-region structures should have formed with comparable scales to those reported here and with growth rates on the order of seconds.

At auroral latitudes the application is not so clear because the chemical damping term, αn_o, is larger than at midlatitudes owing to particle precipitation. Exceptions might be in the winter polar cap or in the region just equatorward of the diffuse auroral zone where the E-region density should be comparable to midlatitude values.

IV SUGGESTIONS FOR FUTURE WORK

The results we have outlined from the past year's work have spanned a large area of theoretical and experimental physics. It is clear that the area least understood in both the natural and the nuclear environments is high-latitude plasma structure phenomenology. During this year we intend to concentrate principally on this area, making heavy use of data from the HILAT satellite in conjunction with incoherent-scatter radar and spaced-receiver measurements. We will develop theoretical models to guide the interpretation of the experimental data; where possible, we will use these models to simulate nuclear effects at high latitudes. One simple but nevertheless fundamental question that we will address is the role of the magnetosphere in prolonging or enhancing the development of structure in the nuclear-disturbed environment. Such prolongation might be expected because destabilizing magnetospheric field-aligned currents will be intensified at the edges of the strong conductivity enhancement produced by the detonation. Another direct application of our magnetospheric convection model will be to predict where nuclear-produced debris ionization will be distributed at very late times. The redistribution will, of course, be a strong function of the latitude and local time of the detonation.

Further refinement and verification of our developing models, as well as those of others, will be carried out through extensive analysis of data on naturally occurring F-layer structure from HILAT. We have previously presented a framework for understanding the morphology of naturally occurring high-latitude irregularities [Vickrey, 1982; DNA La Jolla Conference, 1982; Vickrey and Kelley, 1982; Kelley et al., 1982]. The framework consists of accurately specifying: the latitude-local-time "source function" of irregularity production, the (scale-size dependent) lifetime of irregularities once produced, and the redistribution of structured plasma during its lifetime by magnetospheric convection. Although this framework is straightforward, each individual element is very complex but can be addressed using HILAT data. Listed below are brief descriptions of some of the studies we intend to begin in collaboration with other DNA researchers during the next year. This list is grouped according to our irregularity morphology framework. Obviously, the list is too extensive to be completely fulfilled within one year, but we hope to make substantive progress in most of these foreseeable problem areas.

A. Irregularity Production Studies

1. Global Precipitation Source Function

It is important to characterize accurately the latitude-local-time variations of precipitating particle flux as a function of particle energy. The changes in precipitation characteristics with magnetic activity, in the interplanetary magnetic field direction, in solar wind speed, and in the general state of the magnetosphere should be specified. This study can be accomplished in large part through routine analysis and careful sorting of the particle detector data from HILAT. However, early in the satellite mission the 2-D vacuum ultra violet (VUV) images should be calibrated against the particle detector and incoherent-scatter measurements so that they can be interpreted both in terms of the source function itself and perhaps in specifying the state of the magnetosphere.

2. Spatial Structure of Precipitation

To date, the spectral characteristics of particle precipitation have not been examined in detail--particularly at the soft energies responsible for F-region ionization. It is not known, therefore, if structured precipitation can directly produce structured F-layer ionization at kilometer scales and smaller, or if precipitation is only responsible for the large-scale "seed" features on which instabilities operate. To examine this question, the same spectral analysis techniques that will be applied to the in-situ density data (as well as the beacon, driftmeter, and magnetometer data--see below) should be applied to the particle detector data. In this way the direct contribution of the spatial precipitation spectrum to the in-situ density irregularity spectrum can be immediately assessed.

3. Global Conductivity Distribution

The particle detector and, to some extent, the VUV imager can be analyzed (as in the first study above) to give the latitude-local-time distribution of precipitating particle flux as a function of energy. Using a model neutral atmosphere, this information can be used to derive the ionospheric E-region density profile, and, hence, the conductivity, $\bar{\bar{\Sigma}}$. The importance of determining the E-region conductivity is that it strongly affects both the growth rate of convective instabilities and the diffusive decay of irregularities once produced.

4. Global Characterization of Density Irregularity Spectrum

Some irregularity sources and sinks may be highly scale-size dependent. To examine the interaction of these mechanisms, the entire spectrum of irregularities must be studied as a whole. Moreover, non-linear plasma processes can couple energy between different scale-size regimes. Therefore, a careful spectral analysis of the in-situ density data is essential so that the latitude-local-time variations in the irregularity spectrum, $S(k)$, can be characterized. Evaluation of propagation effects on communications and surveillance systems begins with this characterization.

5. Convection Velocity Shears

Structured electric fields can produce structured plasma density in two principal ways. First, where the electric field, $\bar{E}$, is large, the enhanced ion temperature due to Joule heating affects the F-region chemistry in such a way as to produce a density depletion. At present, we do not know over what scale-size regime this process might operate. Second, a structured electric field can produce structured density by simply mixing flux tubes of different densities. Thus, a turbulent magnetospheric electric field can produce much the same result as a local convective instability. Therefore, it is important that the magnitude, frequency of occurrence, and global distribution of velocity shears be characterized and correlated with regions of density structure.

6. Relationships Between $\bar{E}$ and $\overline{\nabla N}$

An examination of the relationship between $\bar{E}$ and the density gradient ($\overline{\nabla N}$) should give an indication of whether structure at a given scale size is being driven by an instability or is diffusing. In the latter case, theoretical predictions of the relationship between $\delta\bar{E}$ and δN under varying E-region conductivity conditions can be tested; in the instability case, the relationship between these quantities can help identify wave modes; e.g., fluted or nonfluted.

7. Global and Small-Scale Parallel Current Patterns

The field-aligned current magnitude ($J_{\parallel}$), is the driving term in the growth rate expression for the current-convective instability. The sense of the large-scale global patterns of field-aligned current has been studied extensively with TRIAD data, but the magnitude of the currents has not been studied. Moreover, interest has been focused in the past on the global morphology of current systems. Although these large-scale features provide a permanent destabilizing influence, small-scale field-aligned currents may be much more intense. It thus seems worthwhile to apply the same spectral analysis technique used on the density, velocity, and precipitating particle data to the magnetometer data. In that way the magnitude and intensity of small-scale currents can be assessed statistically.

8. Global Empirical Modeling of $\bar{E}$, $\bar{\bar{\Sigma}}$, $J_{\parallel}$, and $\bar{U}$

Indications are that the pertinent instability growth rates in the polar regions are faster than the classical diffusive lifetime of irregularities. This means that growth of structure on a given set of flux tubes is cumulative, to some extent, as those flux tubes convect around the polar regions. The amount of structure on those flux tubes therefore depends on their past history. An assessment of the destabilizing influences suffered during that time can be assessed only by modeling the global patterns of $\bar{E}$, $\bar{\bar{\Sigma}}$, $J_{\parallel}$, and the neutral wind, $\bar{U}$.

9. Comparison of TEC and Scintillation Boundary

The extensive Wideband data set shows that the equatorward TEC boundary is consistently associated with a region of enhanced scintillation-producing irregularities. This relationship merits further investigation with the more extensive diagnostics on board HILAT. It may be possible, for example, to relate the equatorward TEC boundary directly to the equatorward magnetospheric convection boundary.

B. Irregularity Lifetime Studies

1. Global Conductivity Distribution

When the E-region Pedersen conductivity is high, the classical F-region cross-field diffusion rate can be enhanced by an order of magnitude. Also, the pertinent instability growth rates scale by the ratio of F-region to E-region Pedersen conductivity. Thus, the above Global Conductivity Distribution study is pertinent to two of our framework elements.

2. Global Characterization of Density Irregularity Spectrum

To examine irregularity sources and sinks, the entire spectrum of irregularities must be studied as a whole, using data from both the drift meter and multifrequency phase propagation observations. This may reveal scale-size dependent drivers and damping mechanisms. There are some indications that anomalous diffusion operates at high latitudes, but this assumption is based on examining irregularities at only one scale size. If the diffusion is due to, say, drift waves, then it may be highly scale-size dependent.

3. Relationships Between $\bar{E}$ and $\overline{\nabla N}$

As in the source studies just mentioned, if anomalous diffusion is caused by waves in the plasma, then the relationship between $\delta\bar{E}$ and δN will help to identify those waves. If anomalous diffusion is driven by microinstabilities (which produce waves with perturbed $\bar{E}$ on the scale size of the ion gyroradius), then perhaps rocket measurements, in addition to HILAT measurements, would be required to resolve the waves.

4. Global Empirical Modeling of $\bar{E}$, $\bar{\bar{\Sigma}}$, $J_{\parallel}$, and $\bar{U}$

As discussed in A.7 above, structured growth is cumulative. By the same token, if flux tubes convect into regions where the configuration of $\bar{E}$, $\bar{U}$, and $\overline{\nabla N}$ is stabilizing, then structure should be damped.

C. Convection-Driven Redistribution of Structured Plasma

The high-latitude convection pattern is known to depend strongly on the orientation of the interplanetary magnetic field, solar wind speed, and so on. This behavior needs further characterization to ultimately achieve predictive capability. Not only does convection redistribute structured plasma (and perhaps play a role in determining irregularity geometry), but slippage between the convective flow and the neutral wind can produce the structure.

An additional and needed system specification, as well as a helpful clue for understanding nonlinear structure evolution, is the geometry of irregularities. This geometry is undoubtedly scale-size dependent and cannot be determined from the satellite in-situ data alone. Its determination will require different measurements for different scale sizes; e.g., incoherent scatter measurements for $\lambda \geqslant 10$ km, and spaced-receiver measurements for $\lambda \leqslant 1$ km.

Spaced-receiver measurements from HILAT will extend the coverage of kilometer-scale irregularity anisotropy measurements to other local times that Wideband did not sample. Extension of the latitudinal coverage over that of Wideband is also possible. The comparison of data taken from HILAT with data currently being analyzed from quasi-stationary satellites will also help elucidate the differences between temporal and spatial decorrelation of scintillation-producing structure.

Recent measurements (as well as simple theory) [Vickrey, 1982] suggest that irregularity anisotropy may be strongly influenced by the magnetospheric convection pattern. Coordinated measurements taken by spaced-receivers at Sondrestrom, the ion drift meter aboard HILAT, and incoherent-scatter radar can examine this relationship and its scale-size dependence. We also intend to conduct experiments in conjunction with the EISCAT incoherent-scatter facility. Because of its unique capabilities (in particular, its tristatic configuration, Barker coding, lower frequency and increased sensitivity, compared with those of the Chatanika facility), EISCAT may be able to resolve structure in the scale-size regime not covered by the Sondrestrom radar/spaced-receiver measurements; i.e., 1 to 10 km. The tristatic configuration may also allow very direct comparison of irregularity anisotropy and convection streamlines. Moreover, because the density configuration and velocity field can be measured simultaneously with the same resolution, one can immediately assess the growth rate of structure for comparison to theory.

REFERENCES

Aarons, J., "Equatorial Scintillations: A Review," IEEE Trans. Ant. Prop., Vol. 25, No. 5, pp. 729-736 (September 1977).

Aarons, J., J. P. Mullen, J. P. Koster, R. F. da Silva, J. R. Medeiros, R. T. Medeiros, A. Bushby, J. Pantoja, J. Lanat, and M. R. Paulson, "Seasonal and Geomagnetic Control of Equatorial Scintillation in Two Longitudinal Sectors," J. Atmos. Terr. Phys., Vol. 42, No. 9/10, pp. 861-866 (Sept./Oct. 1980).

Aarons, J., H. E. Whitney, E. MacKenzie, and S. Basu, "Microwave Equatorial Scintillation Intensity During Solar Maximum," Radio Sci., Vol. 16, No. 5, pp. 939-945 (Sept./Oct. 1981).

Abdu, M. A., J. A. Bittencourt, and I. S. Batista, "Magnetic Declination Control of the Equatorial F-Region Dynamo Electric Field Development and Spread-F," J. Geophys. Res., Vol. 86, No. A13, pp. 11443-11446 (December 1981).

Bandyopadhyay, P., and J. Aarons, "The Equatorial F-Layer Irregularity Extent as Observed from Huancayo, Peru," Radio Sci., Vol. 5, No. 6, pp. 931-938 (June 1970).

Baron, M. J., C. J. Heinselman, and J. Petriceks, "Solar Cycle and Seasonal Variations of the Ionosphere Observed with the Chatanika Incoherent-Scatter Radar," Paper presented at International URSI Symposium, University of Alaska, Fairbanks, Alaska, 1982.

Basu, S., and S. Basu, "Equatorial Scintillations--A Review," J. Atmos. Terr. Phys., Vol. 43, No. 5/6, pp. 473-489 (May/June 1981).

Basu, S., S. Basu, and B. K. Kahn, "Model of Equatorial Scintillations From in-situ Measurements," Radio Sci., Vol. 11, No. 10, pp. 821-832 (October 1976).

Basu, S., S. Basu, J. P. Mullen, and A. Bushby, "Long-Term 1.5 GHz Amplitude Scintillation Measurements at the Magnetic Equator," Geophys. Res. Letts., Vol. 7, No. 4, pp. 259-262 (April 1980).

Burke, W. J., M. C. Kelley, R. C. Sagalyn, M. Smiddy, and S. T. Lai, "Polar-Cap Electric-Field Structures with a Northward Interplanetary Magnetic Field," Geophys. Res. Letts., Vol. 6, p. 21 (January 1979).

Burke, W. J., D. E. Donatelli, and R. C. Sagalyn, "The Longitudinal Distribution of Equatorial Spread-F Plasma Bubbles in the Topside Ionosphere," J. Geophys. Res., Vol. 85, No. A3, pp. 1335-1340 (March 1980).

Chandra, H., and R. G. Rastogi, "Spread-F at Magnetic Equatorial Station Thumba," Ann. Geophys., Vol. 28, p. 37 (1972).

Chatterjee, S. K., A. K. Bandyopadhyay, B. K. Buhathakurta, and P. Bandyopadhyay, "The Equatorial Scintillation Belt as Observed at Huancayo, Peru," Ann. Geophys., Vol. 30, p. 329 (1974).

Costa, E., and M. C. Kelley, "On the Role of Steepened Structures and Drift Waves in Equatorial Spread-F," J. Geophys. Res., Vol. 83, No. A9, pp. 4359-4364 (September 1978).

Dungey, J. W., "Convective Diffusion in the Equatorial F Region," J. Atmos. Terr. Phys., Vol. 9, p. 304 (1956).

Eather, R. H., "Latitudinal Distribution of auroral and Airglow Emissions: The "Soft" Auroral Zone," J. Geophys. Res., Vol. 74, No. 1, pp. 153-158 (January 1969).

Fang, D. J., and C. H. Liu, "A Morphological Study of Gigahertz Equatorial Scintillations in the Asian Region," submitted to Radio Sci., 1982.

Farley, D. T., Jr., "A Theory of Electrostatic Fields in a Horizontally Stratified Ionosphere Subject to a Vertical Magnetic Field," J. Geophys. Res., Vol. 64, p. 1225 (1959).

Fejer, B. G., and M. C. Kelley, "Ionospheric Irregularities," Rev. Geophys. and Space Phys., Vol. 18, No. 2, pp. 401-454 (May 1980).

Frank, L. A., and K. L. Ackerson, "Observations of Charged-Particle Precipitation into the Auroral Zone," J. Geophys. Res., Vol. 76, No. 16, pp. 3612-3643 (June 1971).

Fremouw, E. J., C. L. Rino, R. C. Livingston, and M. D. Cousins, "A Persistent Subauroral Scintillation Enhancement Observed in Alaska," Geophys. Res. Letts., Vol. 4, No. 11, pp. 542-539 (November 1977).

Friis-Christensen, E., K. Lassen, J. Wilhjelm, J. M. Wilcox, W. Gonzalez, and D. S. Colburn, "Critical Component of the Interplanetary Magnetic Field Responsible for Large Geomagnetic Effect in the Polar Cap," J. Geophys. Res., Vol. 77, No. 19, pp. 3371-3376 (July 1972).

Goldman, S. R., L. Baker, S. L. Ossakow, and A. J. Scannapieco, "Striation Formation Associated with Barium Clouds in an Inhomogeneous Ionosphere," J. Geophys. Res., Vol. 81, No. 28, pp. 5097-5113 (October 1976).

Haerendel, G., "Theory of Equatorial Spread-F," preprint, Mac-Planck Inst. fur Phys. and Astrophys., Inst. fur Extraterr. Phys., Carching, Federal Republic of Germany, 1973.

Harper, R. M., and J. C. G. Walker, "Comparison of Electrical Conductivities in the E- and F-Regions of the Nocturnal Ionosphere," Planet. Space Sci., Vol. 25, No. 2, pp. 197-199 (February 1977).

Heelis, R. A., P. C. Kendall, R. J. Moffett, D. W. Windle, and H. Rishbeth, "Electrical Coupling of the E- and F-Regions and its effect on F-Region Drifts and Winds," Planet. Space Sci., Vol. 22, No. 5, pp. 743-756 (May 1974).

Heelis, R. A., J. K. Lowell, and R. W. Spiro, "A Model of the High-Latitude Ionospheric Convection Pattern," J. Geophys. Res., Vol. 87, No. A8, pp. 6339-6345 (August 1982).

Heppner, J. P., "Polar-Cap Electric-Field Distribution Related to the Interplanetary Magnetic-Field Direction," J. Geophys. Res., Vol. 77, No. 25, pp. 4877-4887 (September 1972).

Hoffman, R. A., and C. S. Lin, "Study of Inverted-V Auroral Precipitation Events," in Physics of Auroral Arc Formation, edited by S.-I. Akasofu and J. R. Kan, Geophys. Mono. 25, American Geophysical Union, Washington, D.C. pp. 80-90, 1981.

Huang, C. M., "F-Region Irregularities that Cause Scintillations and Spread-F Echoes at Low Latitudes," J. Geophys. Res., Vol. 75, No. 25, pp. 4833-4841 (September 1970).

Hudson, M. K., and C. F. Kennel, "Linear Theory of Equatorial Spread F," J. Geophys. Res., Vol. 80, p. 4581 (1975).

Kelley, M. C., G. Haerendel, H. Kappler, A. Valenzuela, B. B. Balsley, D. A. Carter, W. L. Ecklund, C. W. Carlson, B. Hausler, and R. Torbert, "Evidence for a Rayleigh-Taylor Type Instability and Upwelling of Depleted Density Regions During Equatorial Spread-F," Geophys. Res. Letts., Vol. 3, pp. 448 (1976).

Kelley, M. C., K. D. Baker, and J. C. Ulwick, "Late Time Barium Cloud Striations and their Relationships to Equatorial Spread-F," J. Geophys. Res., Vol. 84, No. A5, pp. 1898-1904 (May 1979).

Kelley, M. C., R. Pfaff, K. D. Baker, J. C. Ulwick, R. Livingston, C. Rino, and R. Tsunoda, "Simultaneous Rocket Probe and Radar Measurements of Equatorial Spread-F--Transitional and Short Wavelength Results," J. Geophys. Res., Vol. 87, No. A3, pp. 1575-1588 (March 1982).

Keskinen, M. J., and S. L. Ossakow, "On the Spatial Power Spectrum of the E X B Gradient Drift Instability in Ionospheric Plasma Clouds," J. Geophys. Res., Vol. 86, No. A8, pp. 6947-6950 (August 1981).

Koster, J. R., "Equatorial Scintillation," Planet. Space Sci., Vol. 20, No. 12, pp. 1999-2014 (December 1972).

Krishna Moorthy, K., C. Raghava Reddy, and B. V. Krishna Murthy, "Nighttime Ionospheric Scintillations at the Magnetic Equator," VSSC Tech. Rept. 46, Space Physics Div., Vikram Sarabhai Space Centre, Trivandrum India 695 022, 1978.

Lin, C. S., and R. A. Hoffman, "Characteristics of the Inverted-V Event," J. Geophys. Res., Vol. 84, No. A4, pp. 1514-1524 (April 1979).

Linson, L. M., and J. B. Workman, "Formation of Striations in Ionospheric Plasma Clouds," J. Geophys. Res., Vol. 75, No. 16, pp. 3211-3219 (June 1970).

Livingston, R. C., "Comparison of Multifrequency Equatorial Scintillation: American and Pacific Sectors," Radio Sci., Vol. 15, No. 4, pp. 801-814 (July/August 1980).

Livingston, R. C., C. L. Rino, J. Owen, and R. T. Tsunoda, "The Anisotropy of High-Latitude Nighttime F-Region Irregularities," J. Geophys. Res., Vol. 87, No. A12, pp. 10519-10526 (December 1982).

Lloyd, J. H., and G. Haerendel, "Numerical Modeling of the Drift and Deformation of Ionospheric Plasma Clouds and of their Interaction With Other Layers of the Ionosphere," J. Geophys. Res., Vol. 78, No. 31, pp. 7389-7415 (November 1973).

Maruyama, T., and N. Matuura, "Global Distribution of Occurrence Probability of Spread Echoes Based on ISS-b Observations," J. Radio Res. Labs. (Japan), Vol. 27, p. 201 (1980).

McDonald, B. E., S. L. Ossakow, S. T. Zalesak, and N. J. Zabusky, "Scale Sizes and Lifetimes of F-Region Plasma Cloud Striations as Determined by the Condition of Marginal Stability," NRL Memorandum Report 4383, NRL, Washington, D.C. (1980).

Morse, F. A., B. C. Edgar, H. C. Koons, C. J. Rice, W. J. Heikkila, J. H. Hoffman, B. A. Tinsley, J. D. Winningham, A. B. Christensen, R. F. Woodman, J. Pomalaza, and R. N. Teixeira, "Equion, An Equatorial Ionospheric Irregularity Experiment," J. Geophys. Res., Vol. 82, No. 4, pp. 578-592 (February 1977).

Mozer, F. S., and R. Serlin, "Magnetospheric Electric-Field Measurements with Balloons," J. Geophys. Res., Vol. 74, No. 19, pp. 4739-4754 (September 1969).

Muldrew, D. B., "Characteristics of Ionospheric Bubbles Determined from Aspect Sensitive Scatter Spread-F Observed with Alouette I," J. Geophys. Res., Vol. 85, No. A5, pp. 2115-2123 (May 1980).

Nichols, B. E., "UHF Fading from a Synchronous Satellite Observed at Kwajalein October 1970 through June 1972," Technical Note, 1974-19, AF Contract F19628-73-C-0002, Lincoln Laboratory, Bedford, MA (1974).

AD-A136 396   PHENOMENOLOGY OF STRUCTURED PLASMA IN THE IONOSPHERE   22
(U) SRI INTERNATIONAL MENLO PARK CA J F VICKREY ET AL.
01 MAR 83 DNA-TR-82-104 DNA001-82-C-0021

UNCLASSIFIED   F/G 4/1   NL

END
DATE
FILMED
1-84
DTIC

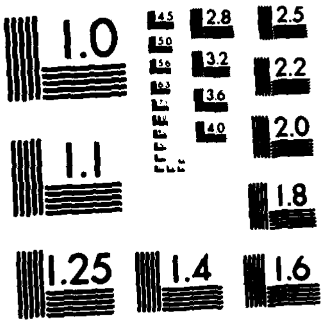

MICROCOPY RESOLUTION TEST CHART
NATIONAL BUREAU OF STANDARDS-1963-A

Ossakow, S. L., "Spread-F Theories--A Review," J. Atmos. Terr. Phys., Vol. 43, No. 5/6, pp. 437-452 (1981).

Ossakow, S. L., and P. K. Chaturvedi, "Current Convective Instability in the Diffuse Aurora," Geophys. Res. Letts., Vol. 6, No. 4, pp. 322-335 (April 1979).

Ossakow, S. L., S. T. Zalesak, and M. J. Keskinen, "A Plausible Hypothesis for Striation Freezing in Ionospheric Plasma Clouds," NRL Memorandum Report 4597, NRL, Washington, D.C. (1981).

Paulson. M. R., "Scintillation of VHF/UHF and L-Band Satellite Signals at Guam," Radio Sci., Vol. 16, No. 5, pp. 877-884 (September/October 1981).

Ragstogi, R. G., "Seasonal and Solar Cycle Variations of Equatorial Spread F in the American Zone," J. Atmos. Terr. Phys., Vol. 42, No. 7, pp. 593-597 (July 1980).

Rino, C. L., and R. C. Livingston, "On the Analysis and Interpretation of Spaced-Receiver Measurements of Transionospheric Radio Waves," Radio Sci., Vol. 17, No. 3, pp. 845-854 (1982).

Rino, C. L., and J. Owen, "The Structure of Localized Nighttime Auroral-Zone Scintillation Enhancements," J. Geophys. Res., Vol. 85, No. A6, pp. 2941-2948 (June 1980).

Rino, C. L., and J. F. Vickrey, "Recent Results in Auroral-Zone Scintillation Studies," J. Atmos. Terr. Phys., Vol. 44, No. 10, pp. 875-887 (1982).

Rino, C. L., R. T. Tsunoda, J. Petriceks, R. C. Livingston, M. C. Kelley, and K. D. Baker, "Simultaneous Rocketborne Beacon and in-situ Measurements of Equatorial Spread F--Intermediate Wavelength Results," J. Geophys. Res., Vol. 86, No. A4, pp. 2411-2420 (April 1981).

Rino, C. L., R. C. Livingston, and S. J. Matthews, "Evidence for Sheetlike Auroral Ionospheric Irregularities," Geophys. Res. Letts., Vol. 5, No. 12, pp. 1039-1042 (December 1978).

Rishbeth, H. "Polarization Fields Produced by Winds in the Equatorial F Region," Planet. Space Sci., Vol. 19, No. 3, pp. 357-369 (March 1971).

Sastri, J. H., and B. S. Murthy, "Spread-F at Kodaikanal," Ann. Geophys., Vol. 31, p. 285 (1975).

Scannapieco, A. J., and S. L. Ossakow, "Nonlinear Equatorial Spread-F," Geophys. Res. Letts., Vol. 3, p. 451 (1976).

Senior, C., "Les Conductivities Ionospheriques et Leur Role Dans La Convection Magnetospherique: Une Etude Experimentale et Theorique," These, L'universite Pierre et Marie Curie, Paris 6, France (1980).

Sharma, R. P., and D. B. Muldrew, "Seasonal and Longitudinal Variations in the Occurrence Frequency of Magnetospheric Ionization Ducts," *J. Geophys. Res.*, Vol. 80, No. 7, pp. 977-984 (March 1975).

Starkov, G. V., "Analytical Representation of the Equatorward Boundary of the Auroral Zone," *Geomag. Aeron.*, Vol. 9, No. 4, p. 614 (1969).

Szuszczewicz, E. P., R. T. Tsunoda, R. Narcisi, and J. C. Holmes, "Coincident Radar and Rocket Observations of Equatorial Spread-F," *Geophys. Res. Letts.*, Vol. 7, No. 7, pp. 537-546 (July 1980).

Taur, R. R., "Ionospheric Scintillation at 4 and 6 GHz," *COMSAT Tech. Rev.*, Vol. 3, p. 145 (1973).

Tsunoda, R. T., "Magnetic Field-Aligned Characteristics of Plasma Bubbles in the Nighttime Equatorial Ionosphere," *J. Atmos. Terr. Phys.*, Vol. 42, No. 8, pp. 743-752 (August 1980).

Tsunoda, R. T., "Time Evolution and Dynamics of Equatorial Backscatter Plumes--1. Growth Phase," *J. Geophys. Res.*, Vol. 86, No. A1, pp. 139-149 (January 1981).

Tsunoda, R. T., and J. F. Vickrey, "Evidence of East-West Structure in Large-Scale F-Region Plasma Enhancements in the Auroral Zone," *J. Geophys. Res.*, submitted 1982.

Tsunoda, R. T., and B. R. White, "On the Generation and Growth of Equatorial Backscatter Plumes--1. Wave Structure in the Bottomside F Layer," *J. Geophys. Res.*, Vol. 86, No. A5, pp. 3610-3616 (May 1981).

Tsunoda, R. T., R. C. Livingston, J. P. McClure, and W. B. Hanson, "Equatorial Plasma Bubbles: Vertical-Elongated Wedges from the Bottomside F Layer," *J. Geophys. Res.*, Vol. 87, No. A11, pp. 9171-9180 (November 1982).

Vickrey, J.F., "On the Morphology of Plasma Density Irregularities in the Auroral F-Region," SRI Topical Report 1, SRI Project 2623, DNA Contract DNA001-81-C-0076 (1982).

Vickrey, J. F., and M. C. Kelley, "The Effects of a Conducting E Layer on Classical F-Region Cross-Field Plasma Diffusion," *J. Geophys. Res.*, Vol. 87, No. A6, pp. 4461-4468 (June 1982a)

Vickrey, J. F., and M. C. Kelley, "Irregularities and Instabilities in the Auroral F-Region," in *High-Latitude Space Plasma Physics*, Plenum Press (1982b).

Vickrey, J. F., C. L. Rino, T. A. Potemra, "Chatanika/TRIAD Observations of Unstable Ionization Enhancements in the Auroral F-Region," Geophys. Res. Letts., Vol. 7, No. 10, pp. 780-792 (October 1980).

Vickrey, J. F., R. R. Vondrak, and S. J. Matthews, "The Diurnal and Latitudinal Variation of Auroral Zone Ionospheric Conductivity," J. Geophys. Res., Vol. 86, No. A1, pp. 65-75 (January 1981).

Vickrey, J. F., R. R. Vondrak, and S. J. Matthews, "Energy Deposition by Precipitating Particles and Joule Dissipation in the Auroral Ionosphere," J. Geophys. Res., Vol. 87, No. A7, pp. 5184-5196 (July 1982).

Walker, G. O., and T. Chan, "A Study of Scintillations at Low Latitudes During a Period from Sunspot Minimum to Sunspot Maximum," J. Geophys. Res., Vol. 75, No. 13, pp. 2517-2528 (May 1970).

Watt, T. M., "Incoherent Scatter Observations of the Ionosphere over Chatanika, Alaska," J. Geophys. Res., Vol. 78, No. 16, pp. 2992-3006 (June 1973).

Weber, E. J., and J. Buchau, "Polar-Cap F-Layer Auroras," Geophys. Res. Letts., Vol. 8, No. 1, pp. 125-128 (January 1980).

Weber, E. J., J. Aarons, and A. L. Johnson, "Conjugate Studies of an Isolated Equatorial Irregularity Region," J. Geophys. Res., Accepted (1983).

DISTRIBUTION LIST

DEPARTMENT OF DEFENSE

Defense Nuclear Agency
ATTN: NAFD
ATTN: RAAE, P. Lunn
ATTN: STNA
ATTN: RAEE
ATTN: NATD
3 cy ATTN: RAAE
4 cy ATTN: TITL

Defense Tech Info Ctr
12 cy ATTN: DD

WWMCCS Sys Engineering Org
ATTN: R. Crawford

DEPARTMENT OF THE ARMY

BMD Advanced Technology Center
ATTN: ATC-R, W. Dickinson
ATTN: ATC-O, W. Davies
ATTN: ATC-T, M. Capps
ATTN: ATC-R, D. Russ

BMD Systems Command
ATTN: BMDSC-HLE, R. Webb
2 cy ATTN: BMDSC-HW

US Army Communications Command
ATTN: CC-OPS-W
ATTN: CC-OPS-WR, H. Wilson

US Army Nuclear & Chemical Agency
ATTN: Library

US Army Satellite Comm Agency
ATTN: Doc Control

DEPARTMENT OF THE NAVY

Naval Ocean Systems Center
ATTN: Code 532
ATTN: Code 5323, J. Ferguson
ATTN: Code 5322, M. Paulson

Naval Research Lab
ATTN: Code 4720, J. Davis
ATTN: Code 7500, B. Wald
ATTN: Code 4780, S. Ossakow
ATTN: Code 4700
ATTN: Code 4780
ATTN: Code 6700
ATTN: Code 4187
ATTN: Code 7950, J. Goodman

Office of Naval Research
ATTN: Code 414, G. Joiner
ATTN: Code 412, W. Condell

DEPARTMENT OF THE AIR FORCE

Air Force Weapons Lab
ATTN: SUL
ATTN: NTYC
ATTN: NTN

DEPARTMENT OF THE AIR FORCE (Continued)

Air Force Geophysics Lab
ATTN: OPR, H. Gardiner
ATTN: OPR-1
ATTN: LKB, K. Champion
ATTN: CA, A Stair
ATTN: PHY, J. Buchau
ATTN: R. Babcock
ATTN: R. O'Neil

Air Force Tech Applications Ctr
ATTN: TN

Air Force Wright Aeronautical Lab
ATTN: W. Hunt
ATTN: A. Johnson

Rome Air Development Center
ATTN: OCS, V. Coyne
ATTN: TSLD

Rome Air Development Center
ATTN: EEP, J. Rasmussen

OTHER GOVERNMENT AGENCIES

Department of Commerce
ATTN: R. Grubb

Institute for Telecomm Sciences
ATTN: L. Berry
ATTN: A. Jean
ATTN: W. Utlaut

DEPARTMENT OF ENERGY CONTRACTORS

Los Alamos National Lab
ATTN: MS 670, J. Hopkins
ATTN: P. Keaton
ATTN: MS 664, J. Zinn
ATTN: T. Kunkle, ESS-5
ATTN: R. Jeffries
ATTN: D. Simons
ATTN: J. Wolcott

Sandia National Labs
ATTN: D. Thornbrough
ATTN: Tech Lib 3141
ATTN: D. Dahlgren
ATTN: Space Project Div
ATTN: Org 4231, T. Wright
ATTN: Org 1250, W. Brown

DEPARTMENT OF DEFENSE CONTRACTORS

Aerospace Corp
ATTN: R. Slaughter
ATTN: J. Straus
ATTN: V. Josephson
ATTN: T. Salmi
ATTN: D. Olsen
ATTN: K. Cho
ATTN: I. Garfunkel

DEPARTMENT OF DEFENSE CONTRACTORS (Continued)

BDM Corp
ATTN: L. Jacobs
ATTN: T. Neighbors

Berkeley Research Associates, Inc
ATTN: C. Prettie
ATTN: J. Workman
ATTN: S. Brecht

Charles Stark Draper Lab, Inc
ATTN: D. Cox
ATTN: A. Tetewski
ATTN: J. Gilmore

Cornell University
ATTN: D. Farley Jr
ATTN: M. Kelly

EOS Technologies, Inc
ATTN: B. Gabbard

General Research Corp
ATTN: B. Bennett

HSS, Inc
ATTN: D. Hansen

Institute for Defense Analyses
ATTN: J. Aein
ATTN: E. Bauer
ATTN: H. Wolfhard
ATTN: H. Gates

JAYCOR
ATTN: J. Sperling

Kaman Tempo
ATTN: DASIAC
ATTN: B. Gambill
ATTN: J. Devore
ATTN: K. Schwartz
ATTN: W. McNamara
ATTN: J. Devore

Kaman Tempo
ATTN: DASIAC

M.I.T. Lincoln Lab
ATTN: D. Towle

Mission Research Corp
ATTN: R. Hendrick
ATTN: F. Fajen
ATTN: R. Kilb
ATTN: R. Bogusch
ATTN: C. Lauer
ATTN: S. Gutsche
ATTN: D. Knepp
ATTN: R. Bigoni
ATTN: Tech Library
ATTN: G. McCartor
ATTN: F. Guigliano

DEPARTMENT OF DEFENSE CONTRACTORS (Continued)

Pacific-Sierra Research Corp
ATTN: E. Field Jr
ATTN: H. Brode, Chairman SAGE
ATTN: F. Thomas

Photometrics, Inc
ATTN: I. Kofsky

Physical Dynamics, Inc
ATTN: E. Fremouw

Physical Research, Inc
ATTN: R. Deliberis

R&D Associates
ATTN: R. Lelevier
ATTN: W. Karzas
ATTN: W. Wright
ATTN: R. Turco
ATTN: M. Gantsweg
ATTN: H. Ory
ATTN: C. Greifinger
ATTN: F. Gilmore

R&D Associates
ATTN: B. Yoon

SRI International
ATTN: V. Gonzales
ATTN: W. Chesnut
ATTN: D. McDaniels
ATTN: M. Baron
ATTN: R. Leadabrand
ATTN: G. Price
ATTN: D. Neilson
ATTN: A. Burns
ATTN: W. Jaye
ATTN: J. Petrickes
ATTN: G. Smith
4 cy ATTN: R. Tsunoda
4 cy ATTN: J. Vickrey
4 cy ATTN: R. Livingston
4 cy ATTN: C. Rino
4 cy ATTN: R. Robinson
4 cy ATTN: M. Cousins
4 cy ATTN: N. Walker

Stewart Radiance Lab
ATTN: J. Ulwich

Technology International Corp
ATTN: W. Boquist

Toyon Research Corporation
ATTN: J. Isle
ATTN: J. Garbarino

Visidyne, Inc
ATTN: O. Shepard
ATTN: W. Reidy
ATTN: C. Humphrey
ATTN: J. Carpenter